OPEN ACCESS

One Solar Cycle of Heliosphere Observations with the Interstellar Boundary Explorer: Energetic Neutral Hydrogen Atoms Observed with IBEX-Lo from 10 eV to 2 keV

A. Galli[1] , P. Wurz[1] , N. A. Schwadron[2] , K. Fairchild[2], D. Heirtzler[2], E. Möbius[2] , H. Kucharek[2], R. Winslow[2] ,
M. Bzowski[3] , M. A. Kubiak[3] , I. Kowalska-Leszczyńska[3] , S. A. Fuselier[4] , J. M. Sokół[5] , P. Swaczyna[6] , and
D. J. McComas[6]

[1] Physics Institute, University of Bern, Bern, 3012, Switzerland; andre.galli@space.unibe.ch
[2] University of New Hampshire, Durham, NH 03824, USA
[3] Space Research Centre, Polish Academy of Sciences, Warsaw, 00-716, Poland
[4] Southwest Research Institute and University of Texas, San Antonio, TX 78228, USA
[5] Southwest Research Institute, San Antonio, TX 78228, USA
[6] Department of Astrophysical Sciences, Princeton University, Princeton, NJ 08544, USA

Abstract

The Interstellar Boundary Explorer (IBEX) is a NASA satellite in Earth orbit, dedicated to observing both interstellar neutral atoms entering the heliosphere and energetic neutral atoms (ENAs) from the interstellar boundaries from roughly 10 eV to 6 keV. This work presents the averaged maps, energy spectra, and temporal variability of heliospheric ENA intensities measured with the IBEX-Lo instrument at 1 au at energies between 10 eV and 2 keV, covering one entire solar cycle from 2009 through 2019. These results expand the range in time and energy for studying the globally distributed ENA flux and the IBEX Ribbon. The observed ENA intensities exceed model predictions, in particular below 500 eV. Moreover, the ENA intensities between 50–200 eV energy show an unexpected rise and fall around the year 2015 in most sky regions.

Unified Astronomy Thesaurus concepts: Heliosphere (711); Heliosheath (710)

1. Introduction

The Interstellar Boundary Explorer (IBEX) has been continually observing the interaction of the heliosphere with the surrounding interstellar medium since the start of science operations in January 2009 (McComas et al. 2009a). IBEX orbits the Earth at distances between 48,000 and 320,000 km, measuring neutral atoms from the heliosphere and from the interstellar medium at energies from roughly 10 eV to 6 keV. The scientific payload consists of two instruments, IBEX-Lo (Fuselier et al. 2009b) and IBEX-Hi (Funsten et al. 2009). IBEX-Lo is sensitive both to heliospheric energetic neutral atoms (ENAs) between 10 eV and 2 keV and to interstellar neutrals.

ENA measurements are a unique tool for remote sensing of space plasma: ENAs are created in a charge exchange between fast ions and ambient neutral atoms and then leave their place of origin on straight trajectories, not affected by local electromagnetic fields. This way, they can cross the full distance from the heliosphere boundaries at 100–150 au to the IBEX spacecraft at 1 au. The ENAs observed by IBEX-Lo may originate from solar wind and pickup ions in the heliosheath and also from ions neutralized outside the heliopause. The low-energy part of the heliospheric ENA spectrum, well below the solar wind energy, is accessible only by IBEX-Lo. This part of the spectrum is crucial for assessing the total plasma pressure in the heliosheath (Fuselier et al. 2012, 2014; Galli et al. 2016, 2017) and for observing the relative importance of different ion acceleration processes in the heliosphere (Desai et al. 2014; Zirnstein et al. 2014, 2018b).

In this paper, we summarize the heliospheric ENA observations obtained with IBEX-Lo over one full solar cycle from the beginning of science operations in 2009 until the end of 2019 for ENA energies from 10 eV to 2 keV. This overview complements the paper by McComas et al. (2020) that summarized the results of the same 11 yr of IBEX-Hi ENA observations covering energies from 0.5 keV to 6 keV. We first present the 11 yr IBEX-Lo data set (Section 2) and list the details of the map selection and processing steps (Section 3). We then summarize the most important ENA products derived from these data: annual and average ENA intensity maps, ENA energy spectra, and time series over the 11 yr (Section 4). We conclude this paper with a discussion of two open questions and the conclusions (Sections 5 and 6).

2. Data Set

IBEX-Lo is a single-pixel camera that observes ENAs from the heliosphere and interstellar neutrals (ISN; Fuselier et al. 2009b). Neutral atoms enter the instrument through a collimator, which defines the field of view of $6°.5 \times 6°.5$. After the collimator, neutral atoms hit a conversion surface where they are reflected with a fraction of the reflected particles being negatively charged. These ions then pass through an electrostatic analyzer and are accelerated into a time-of-flight (TOF) mass spectrometer, which features triple coincidence detection. IBEX-Lo detects negative ions in eight different energy bins or energy steps described as Lo-1 to Lo-8 with the central energies at 0.015, 0.029, 0.055, 0.11, 0.209, 0.439, 0.872, and 1.821 keV. The transmission of the electrostatic analyzer is approximately a log-normal distribution with a $\Delta E/E$ of 0.7 (FWHM divided by peak energy) for all eight energy bins (Fuselier et al. 2009b).

In nominal operations, the electrostatic analyzer cycles through each of the eight energy bins at equal time intervals.

Table 1
Overview of Data Set: 11 yr of IBEX-Lo Heliospheric ENA Data

Year	PAC Voltage	Orbits Included
2009	Nominal	11–58 (without 32–48)
2010	Nominal	59–106 (without 62, 81–101)
2011	Nominal	107–150a (without 110–114 and 128–144)
2012	Nominal	150b–190b (without 150b–155 and 170–182)
2013	Reduced	191a–230b (without 207, 210–222)
2014	Reduced	231a–270b (without 250–261)
2015	Reduced	271a–310b (without 289–300, 303, 304)
2016	Reduced	311a–351a (without 316–317, 323, 329–339)
2017	Reduced	351b–391a (without 368–380, 390)
2018	Reduced	391b–431b (without 405, 408–418)
2019	Reduced	432a–471b (without 441, 446, 448–460)

Note. From 2011 October onward, orbits are evaluated in two separate halves, a and b.

For each energy bin, an onboard algorithm collects blocks of roughly 15 minutes of triple coincidence hydrogen and oxygen counts that pass several quality criteria. Three TOF measurements are combined to verify that a count was due to a true H^- or O^- ion entering the TOF unit at the expected speed given the measured mass. This excludes many counts caused by electrons or UV photons and greatly enhances the signal-to-noise ratio (S/N) (Möbius et al. 2007). For nominal energy stepping, there are 2×8 data blocks of triple coincidence counts of H^- and O^- in the eight energy steps for each 15 minute segment. In this paper we concentrate on the H^- ions.

The observation times for this study include all IBEX-Lo triple coincidence H^- measurements of hydrogen ENAs, yielding annual maps of the heliospheric ENAs from December 2008 until December 2019 (see Table 1). Only observation times of heliospheric ENA data with acceptable quality are included (i.e., covered by the Good Times list; see Section 3). Observations of the Earth's magnetosphere and data during the magnetospheric background season, when the entire IBEX orbit remained inside Earth's bow shock, are excluded from all maps.

Over the 11 yr, instrument efficiencies changed two times: Starting from orbit 169, the throughput of registered counts was improved by modifying the onboard algorithm to accept only those count events with a valid TOF2 time. Shortly after, in orbit 177 (2012 June), the postacceleration (PAC) high voltage of the TOF detector had to be reduced from 16 kV to 7 kV, which reduced the TOF efficiency. Both changes are corrected for in the present data products (see Section 3).

Because of limited statistics at low ENA energies, the finest spatial resolution of the maps is limited to $6° \times 6°$ pixels. Due to a star tracker anomaly in May 2016, the pointing from orbit 326 onward is affected by an offset of $0°.6$ (Swaczyna et al. 2022). This is not an issue for ENA maps and derived products because this uncertainty is much smaller than the statistical scatter. Orbits including data with despun pointing information are also included in the ENA data set to enhance statistics. Despinning may become necessary when the IBEX star tracker is blinded, and the spin phase of the spacecraft drifts as a consequence. The affected data can be corrected (i.e., despun) based on the star sensor data. This despinning removes the drift to a large extent but the process introduces pointing inaccuracies on the order of $0°.1$. For that reason, despun data are usually omitted from ISN-related studies (see, e.g., Swaczyna et al. 2022). This inaccuracy is not an issue

for heliospheric ENA studies because the finest spatial resolution is $6° \times 6°$. The temporal resolution of the IBEX-Lo ENA maps is one full year, compared with the six months for IBEX-Hi ENA maps (McComas et al. 2020). This difference is due to the fact that IBEX-Lo maps have a lower S/N than those obtained with IBEX-Hi for an equal duration of observation time (McComas et al. 2020), in particular for antiram directions at lower energies. Therefore, ram and antiram maps are usually prepared separately. Ram maps are derived from the pixels observed from the hemisphere for which the IBEX-Lo field of view and the spacecraft motion (with respect to the solar inertial frame) align whereas the IBEX-Lo hemisphere facing away from the spacecraft motion is used to generate the antiram maps. The transitions between ram and antiram occur mid-bin toward the ecliptic South and North poles; the row of pixels from $84°...90°$ and $-84°...-90°$ thus appear both in ram and in antiram maps.

The IBEX Science Operations Center (SOC) and the authors of this study have released the data sets related to this study.[7] The map names used by the SOC for the different map products are stated in Table 2.

3. ENA Mapping Method

The processing sequence implemented by the SOC to produce ENA intensity maps from raw count rates measured with IBEX-Lo is listed here. Steps 9 and 11 are needed only for ENA intensities transformed to the solar inertial reference frame at 100 au heliocentric distance. The following sequence is valid for the data products presented in the results section. Some additional comparisons between alternative mapping methods are discussed in Appendix A. One step absent from this list is the subtraction of the count rates caused by the ISN helium and hydrogen from the ENA maps in energy bins 1–4 around the ISN inflow direction. Such an approach would require a specific model of ISN He, which has to take into account all the physics of ISN He and H outside and inside the heliosphere (see, e.g., Kubiak et al. 2014; Galli et al. 2019; Swaczyna et al. 2022). Because the ISN He inflow creates orders of magnitude more count rates than the ENA signal at low energies (see the wedge-shaped areas of high count rates in Figure 3), Poisson uncertainties in pixels dominated by this ISN signal are larger than the underlying ENA signal. Therefore, minor inaccuracies in the ISN model would lead to a gross overestimation or complete erasure of other components of the signal. The resulting corrected ENA map thus would critically depend on specific model assumptions. This is not desirable for an overview of maps and data release that are to serve as the starting point for model work. We will therefore concentrate (in Section 4) on ENA maps at energy bins 5–8 and will only discuss ENA measurements at lower energy bins in the context of energy spectra for sky regions outside the ISN inflow.

1. Apply the list of quiet observation times (the so-called "Good Times") and combine it with the request that a valid data block of 15 minutes must have less than four counts per half arc of IBEX spin (one half arc or hemisphere containing 30 pixels that cover the ram or the antiram hemisphere) both in energy bins 7 and 8. The result is the "Super Good Times" list, based on the same criteria as the approach used by Fuselier et al. (2014) and Galli et al. (2014). Energy bins 7 and 8 are used because IBEX-Lo is most sensitive to magnetospheric and solar

---

[7] https://ibex.princeton.edu/DataRelease17

Table 2
Available Sets of Hydrogen ENA maps

Short Name in Paper	SOC Name	Ram?	Postprocess.	Comments
SC-Ram-Maps	lvset_h_noSP_ram_hb	Ram	None	**Default ENA maps**
CG-Maps	lvset_h_cg_hb	All	CG	
CG-Ram-Maps	lvset_h_noSP_ram_cg_hb	Ram	CG	
CG-Antiram-Maps	lvset_h_noSP_antiram_cg_hb	Antiram	CG	
CG-SP-Ram-Maps	lvset_h_tabular_ram_cg_hb	Ram	CG & SP	**Basis for energy spectra**
CG-SP-Antiram-Maps	lvset_h_tabular_antiram_cg_hb	Antiram	CG & SP	**Needed to check spectra**
CG-SP-Maps	lvset_h_tabular_cg_hb	All	CG & SP	**Needed to check spectra**

Note. "SC" = in the spacecraft reference frame, "CG" = corrected for Compton–Getting, and "SP" = corrected for survival probability.

wind background around the solar wind energy. Demanding, in addition, low TOF2 count rates during observation periods would result in a "Super Better Times" list (Galli et al. 2016, 2017), rejecting a few incidences with high count rates while further reducing observation time periods and thus count statistics (see Appendix A). For this paper and data release on heliospheric ENAs, we used only the "Super Good Times" list.

2. Correct for spin bin 0 exposure: The electrostatic analyzer cycles through the eight IBEX-Lo energy bins in a pattern of 1-2-3-4-5-6-7-8-1, etc. After the highest energy (energy bin 8), the voltages of the electrostatic analyzer are readjusted to the lowest energy bin 1, which leads to ENAs of higher energies spilling into energy bin 1. Therefore, only the second spin is used for spin bin 0 in energy bin 1, which reduces the exposure time of this bin by a factor of 2 compared to all other bins.

3. Select H^- triple coincidence events, i.e., the data product with the highest S/N for hydrogen ENAs, and create orbit-by-orbit files of H^- count rates. One orbit (or half orbit from 2011 October onward) is the finest time resolution for this analysis and for the corresponding data release. For step 7, also prepare the corresponding files of O^- count rates.

4. Apply the throughput correction before orbit 169 (divide raw count rates by [0.93, 0.93, 0.88, 0.76, 0.87, 0.95, 0.96, 0.96] for energy bins 1 to 8, respectively) or apply the PAC change related efficiency correction from orbit 177 onward (count rates are divided by factors of [0.43, 0.44, 0.44, 0.44, 0.45, 0.47, 0.51, 0.58] for energy bins 1 to 8, resp.). These are the same correction factors used for previous ENA and ISN H studies (Galli et al. 2017, 2019).

5. Subtract ubiquitous background from raw count rates and correct variance accordingly. This ubiquitous background is restricted mostly to the energy bins below 200 eV (Galli et al. 2015, 2017). See Appendix B for more details.

6. Create differential energy flux files using laboratory calibration data and update variance files. This concludes the conversion into physical units.

7. Correct for the potential contribution of ISN oxygen (which may sputter H^- off the conversion surface) to pixels close to the ISN inflow in energy bins 5 and 6: This is only applicable to orbits before 177 when the oxygen count rates were reliable as a result of the high PAC voltage. After this orbit, no oxygen correction is applied because the instrument no longer detects O^- efficiently enough. For this correction, the ubiquitous O^- background is subtracted from the O^- count rates (see Table 9 in Appendix B).

8. Correct for sputtering products from higher-energy H atoms: The sputtering correction based on the bootstrap method (refer to Table 5 in McComas et al. 2014) is applied. This implies that files from IBEX-Hi energy bin 5 are needed for correcting IBEX-Lo energy bins 5–8. No sputtering correction is applied to energy bins 1–4. It was verified that this does not introduce a spurious jump in energy spectra between energy bins 4 and 5 (see Section 4.3).

9. Apply Compton–Getting (CG) correction to compensate for spacecraft proper motion: this is achieved by obtaining the direction-dependent energy for a given pixel, resulting in corrected ENA intensities at nonuniform energies for different directions (McComas et al. 2010).

10. Calculate the S/N and create associated maps.

11. Correct for the energy-dependent ENA survival probability (SP) to conclude postprocessing: The measured ENA intensities are corrected for the re-ionization losses they suffered on their trajectory from the heliosheath region at 100 au to the spacecraft at 1 au heliocentric distance. The details on the survival probabilities are described in Appendix C, the methodology is provided by Bzowski (2008). Since previous studies on heliospheric ENA intensities measured with IBEX-Lo (Galli et al. 2016, 2017), the ionization rates (Sokół et al. 2020) and the model of radiation pressure (Kowalska-Leszczyńska et al. 2020) have been updated. As a consequence, the derived ENA intensities in the present study are consistently higher than in the previous studies because of the decreased survival probability at low energies for off-ecliptic pointing (Sokół et al. 2020).

4. Results

We first present the annual ENA intensity maps (for the optimum combination as derived in the previous section) for all individual 11 yr (Section 4.1), followed by 11 yr averages (Section 4.2), energy spectra (Section 4.3), and quantification of any temporal changes (Section 4.4).

The following complete sets of hydrogen ENA maps are at our disposal and are part of the data release (Table 2).

4.1. Year-by-year Maps

Figure 1 shows the year-by-year SC-Ram-Maps (see Table 2) of ENA intensities, in analogy to Figures 1 and 2 in McComas et al. (2020) for IBEX-Hi data. These maps are provided in Mollweide projection and are centered on the ISN inflow direction at $(\lambda_\infty, \beta_\infty) = (255°7, 5°1)$ (McComas et al. 2015), indicated as

"Nose" between the Voyager 1 ("V1") and Voyager 2 ("V2") directions. Only the annual maps for energy bins 5–8 are shown here, because the maps at the lower energy bins 1–4 (below 200 eV) are dominated by the intense signal of interstellar neutral helium and hydrogen (see Section 4.2). Because antiram observations and observations from within the Earth's bow shock were excluded from these maps, roughly one third of the area within these sky maps are depicted in black. Other gaps in coverage in energy bin 5, e.g., occurred in later years when ISN observations in energy bins 1 and 2 were prioritized over ENA measurements. Even without further averaging or postprocessing the maps, the IBEX Ribbon of enhanced ENA intensities (Fuselier et al. 2009a; McComas et al. 2009b) is visible against the vast stretches of dark blue pixels (the globally distributed ENA flux (McComas et al. 2009b; Schwadron et al. 2014)) in energy bins 6, 7, and 8 during low and medium solar activity (years 2009–2012 and again in 2017–2019). The Ribbon becomes harder to discern in energy bin 5 and generally during high solar activity in 2013–2016. Another prominent feature visible in these maps is the brightening and subsequent dimming of most sky regions in energy bin 5 at roughly 200 eV around the year 2015 (see time series for various sky regions in Section 4.4).

For each annual map in Figure 1, three accompanying maps describe the statistical properties of the ENA intensity maps: pixel exposure, the S/N per pixel, and the variance of the intensity per pixel. Figure 2 shows examples of the S/N maps for energy bins 5–8 for one year (2009) with a comparatively high S/N (low solar activity) and good coverage. The typical S/N is on the order of unity for many pixels. Map pixels in the same year at lower energies where the signal is dominated by the intense ISN have typical S/N of 10–40. Excluding individual intensity pixels based on these statistical properties was investigated: excluding pixels with pixel exposure <0.2 maximum(pixel exposure) or variance >0.2 maximum(variance) or S/N < 1.0, which is equivalent to demanding sqrt (variance) < ENA intensity. However, none of these statistical approaches could remove the bright stripes at the edges of some maps in Figure 1 caused by magnetospheric particles because these contributions are background signals and not random noise. Moreover, any exclusion criterion is arbitrary to some extent and excluding map pixels further aggravates the low statistics with IBEX-Lo ENA observations. A priori, we use all available pixels from the annual maps as shown in Figure 1 and will only use statistical criteria for the 11 yr average maps and the macropixel energy spectra to exclude outliers from those averages.

4.2. The Global Picture over 11 Years

Averaging over the annual ENA intensity maps from the previous section, we calculated the ENA maps averaged over one full solar cycle from 2009 to 2019. The results are shown for all eight energy bins in Figures 3 and 4. These are the arithmetic pixel-by-pixel means over all years. The left columns show the average ENA intensities, the right columns show the relative variability over 11 yr (defined in Equation (1)). Pixels that meet one or several of the following criteria were excluded from the averages: (1) Pixels with relative variability exceeding 0.5, whereby the relative variability is defined as the statistical standard deviation σ_j over all available annual values (usually $N = 11$)

divided by the square root of N times the average intensity $\langle j \rangle$,

$$\frac{\sigma_j}{\sqrt{N}\langle j \rangle} > 0.5, \ N$$
$$= 0, \ldots 11 \text{ (number of annual maps covering this pixel)},$$

(1)

(2) pixels covered only once or never within the 11 yr ($N < 2$), and (3) pixels with an annual flux samples exposure weight <0.15 maximum exposure. Pixels that were excluded based on these criteria are treated as not observed (white pixels in Figure 3 and 4) and are excluded from all further investigation.

The ecliptic longitudes from 0° to 100° were never covered with ram observations outside the magnetospheric season in any of the 11 yr of IBEX-Lo observations (see white pixels in Figures 3 and 4). The bright stripes at the polar pixels around longitude 320° in energy bin 8 (bottom panel of Figure 4) are spillovers of the foreground encountered in the IBEX-Lo hemisphere pointed toward Earth's magnetosphere (the affected hemispheres are excluded from the data via the Good Times list). The maps at energy bins 5–8 (Figure 4) above 150 eV are composed mostly of the globally distributed ENA flux plus the ENA Ribbon bending across the ecliptic plane (see Galli et al. (2022) and references therein for a review of IBEX observations and interpretations of the globally distributed flux and the Ribbon). The ENA Ribbon in IBEX-Lo maps is most conspicuous at 0.9 keV and becomes less prominent against the globally distributed ENA flux at both higher and lower energies (see Section 4.3). The FWHM of the Ribbon increases from $35° \pm 10°$ at 1.8 and 0.9 keV to $50° \pm 10°$ at 0.4 and 0.2 keV (assessed at the Ribbon macropixel as defined in Table 3). At energies below 150 eV, the maps are dominated by the He and H ISN signal centered at ecliptic coordinates 225°/5° (see the bright wedge increasing in size as the energy decreases in Figure 3). This peak position at 1 au is shifted with respect to the inflow direction at infinity due to the gravitational deflection of ISN atom trajectories approaching the Sun. The reconstructed inflow direction of the primary He ISN at infinity is determined from these IBEX-Lo measurements to be $\lambda_\infty = 255°59 \pm 0°23$, $\beta_\infty = 5°14 \pm 0°08$ (see Swaczyna et al. (2022) and earlier publications by Bzowski et al. 2015; McComas et al. 2015; Schwadron et al. 2015). To discuss the heliospheric ENAs, we concentrate on sky regions and energy spectra outside this region in the following. We note, however, that ISN He below 150 eV (bins 1–4) and ISN H below 40 eV (bins 1 and 2) may have added to the observed H$^-$ count rates interpreted as heliospheric ENAs. In energy bins 5 and 6 (i.e., between 150 and 600 eV), the ISN oxygen and neon were observed to produce both H$^-$ and O$^-$ counts in the years 2009–2012 before the PAC change reduced the IBEX-Lo sensitivity to heavy ISN species. The observed Ne and O signal appeared, in the spacecraft reference frame, in the map pixels beside the nose at ecliptic coordinates ($\lambda_{ecl} = 210°...240°$, $\beta_{ecl} = -15°...20°$; Park et al. 2016). During the first 4 yr of IBEX-Lo observations, this potential ISN Ne and O contribution to the maps of heliospheric hydrogen ENAs is eliminated by the oxygen correction (processing step 7). For the maps after the PAC change, it is not possible to apply this method because no useful oxygen count maps are generated. However, a comparison of the region ($\lambda_{ecl} = 210°...240°$, $\beta_{ecl} = -15°...20°$) in the annual maps in energy bin 6 (Figure 1) shows no spurious bright spot appearing in 2018 or 2019 compared with the years 2009 and 2010.
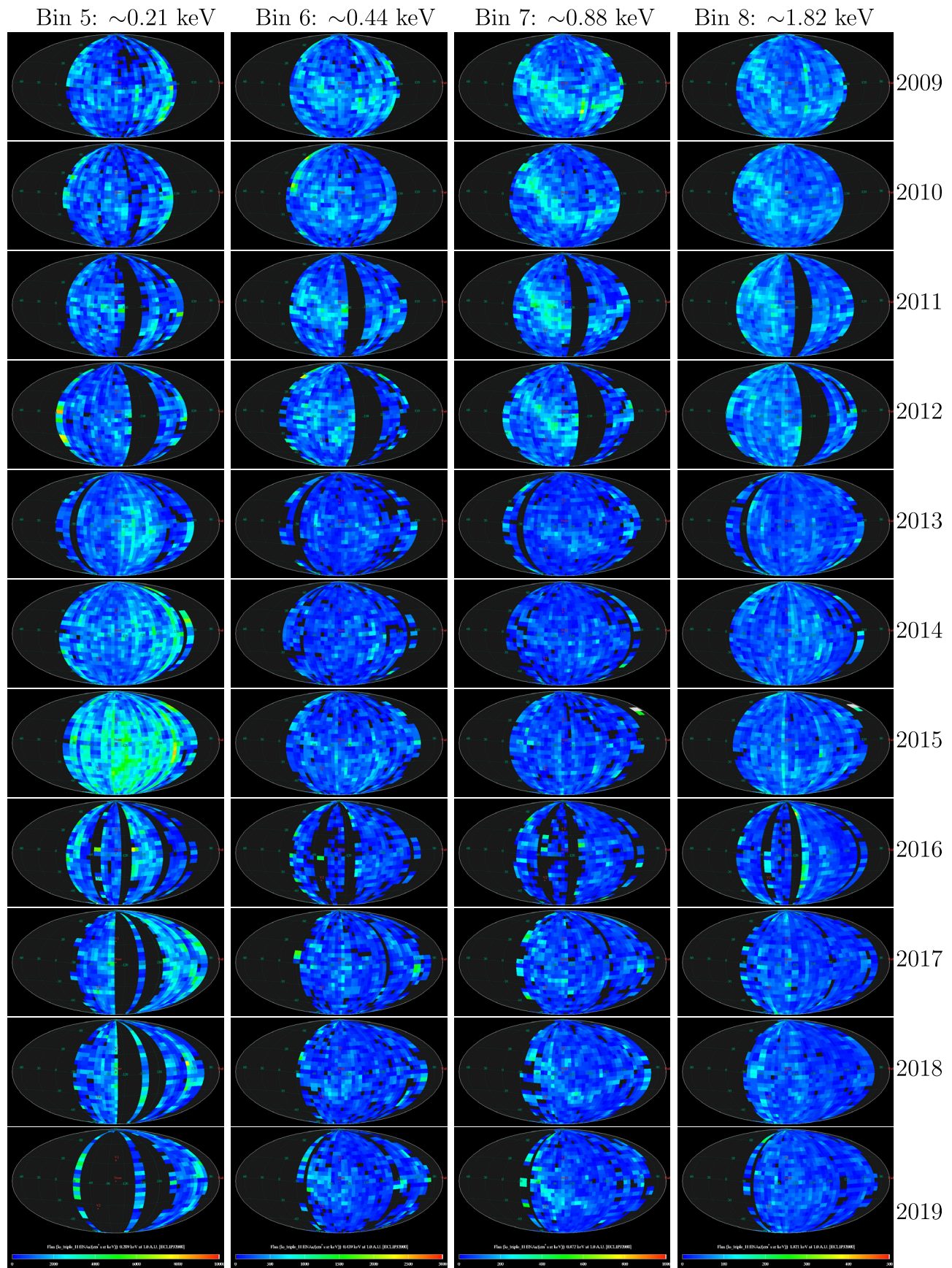
Figure 1. Year-by-year ENA intensity maps (in units of cm^{-2} sr^{-1} s^{-1} keV^{-1}) in the spacecraft reference frame without correction for the survival probability; ram observations only.
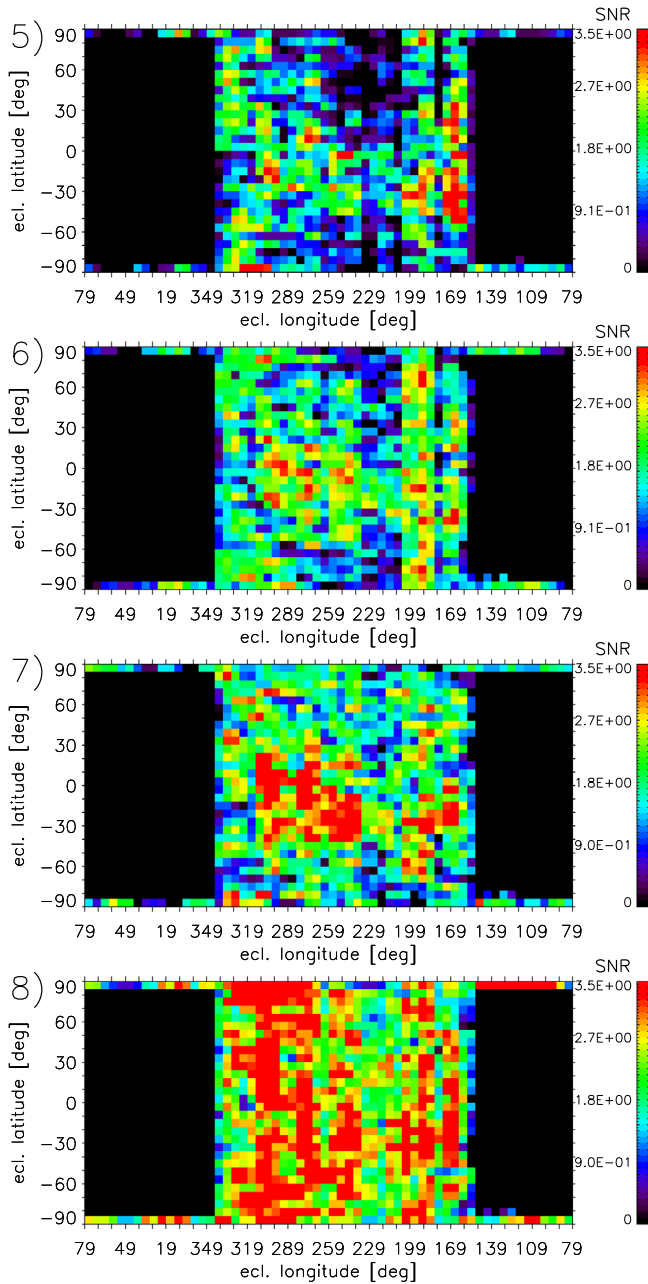
Figure 2. S/N ratios of individual map pixels for the year 2009 for energy bins 5–8.

With Figures 3 and 4 in mind, we define the nine different sky regions illustrated in Figure 5 and described in Table 3. All of them contain 16 6° × 6° map pixels with the exception of the North Pole and South Pole regions that contain 60 map pixels each. The pixels from 84°...90° and −84°... −90° were omitted from the selection because of the potential magnetospheric foreground (see bottom panel in Figure 4). These sky regions only partially correspond to the regions defined in McComas et al. (2020) because they are optimized for the availability of data and low S/N in IBEX-Lo ENA maps and they are chosen to avoid the center of the primary ISN He and Ne and O inflow region around 225° ecliptic longitude and 5° latitude (red regions in Figure 3). The one obvious exception is the Ribbon macropixel, which is strongly affected by the ISN signal. In addition, the Voyager 1 and 2 regions may be affected by the

broad ISN He and H inflow in energy bins 1 and 2 (see Section 4.3). The energy spectrum of the all-sky average would be a combination of several completely different signals (the globally distributed flux, the ENA Ribbon and, below 150 eV, the intense ISN signal). Moreover, energy shifts due to Compton–Getting transformation can be estimated only for a particular region in the sky, which means we cannot attribute a well defined energy to an all sky energy spectrum once Compton–Getting is done. We therefore do not discuss the all-sky average spectrum. We will use the nine selected sky regions to discuss the energy spectra and temporal variations in the two following sections. Note, however, that the Downwind and the Port Tail Lobe regions were only covered with antiram observations.

4.3. Energy Spectrum of Heliospheric ENAs over 11 Years

Based on the 11 yr average maps presented in the previous section, energy spectra for the different sky regions were calculated for all available map types. Pixels with excessive year-to-year variability or too short exposure times were thus excluded. We concentrate on energy spectra derived from SC-Ram-Maps (in the spacecraft reference frame, without survival probability correction) and on CG-SP-Ram-Maps (inertial reference frame, corrected for survival probability). The averaging over several years is unavoidable because of poor statistics and large observational gaps in individual years, although this may fold temporal variability (if present, see Section 4.4) into the averaged spectrum. The result for the ENA intensities in SC-Ram-Maps is shown in Figure 6. The sputtering removal algorithm did not introduce a spurious jump to higher ENA intensities from energy bin 5 to 4. The enhancement due to the IBEX Ribbon (red line) is prominent at solar wind energies, whereas the intensity (for this small subregion of the Ribbon) starts to blend in with the globally distributed ENA flux at other sky regions at 1.8 keV and at 0.4 keV. The spectral shape below 200 eV should not be overinterpreted from this figure because these spectra do not include survival probabilities nor Compton–Getting transformation, which differ markedly for the different sky regions at low energies. The error bars in this figure represent only the standard deviation of the average intensity derived from the spatial variability within the sky region. The excess of apparent ENA intensities in the red energy spectrum below 100 eV is caused by the intense ISN signal (see red spot in Figures 3) and has nothing to do with Ribbon ENAs. Entries from the lowest energy bin are omitted from all spectra because the uncertainties introduced by the vast ISN inflow (see top panel in Figure 3) plus the uncertainties introduced by the Compton–Getting transformation and survival probability become larger than the derived intensities at the lowest energies.

To interpret the ENA energy spectra in a more quantitative way at lower energies and to compare them to the previously published energy spectrum at low ENA energies (Fuselier et al. 2014; Galli et al. 2014, 2016, 2017), we must rely on the CG-SP-Ram-Maps corrected for ENA survival probability and with the Compton–Getting transformation (see Table 2). Furthermore, we must bear in mind that all the aforementioned energy spectra were derived for the first 4 or 6 yr of IBEX-Lo observations only, and the ENA survival probabilities assumed by Galli et al. (2016, 2017) and earlier studies (required to transform the measured ENA intensities to a heliocentric distance of 100 au) were then revised based on improved solar
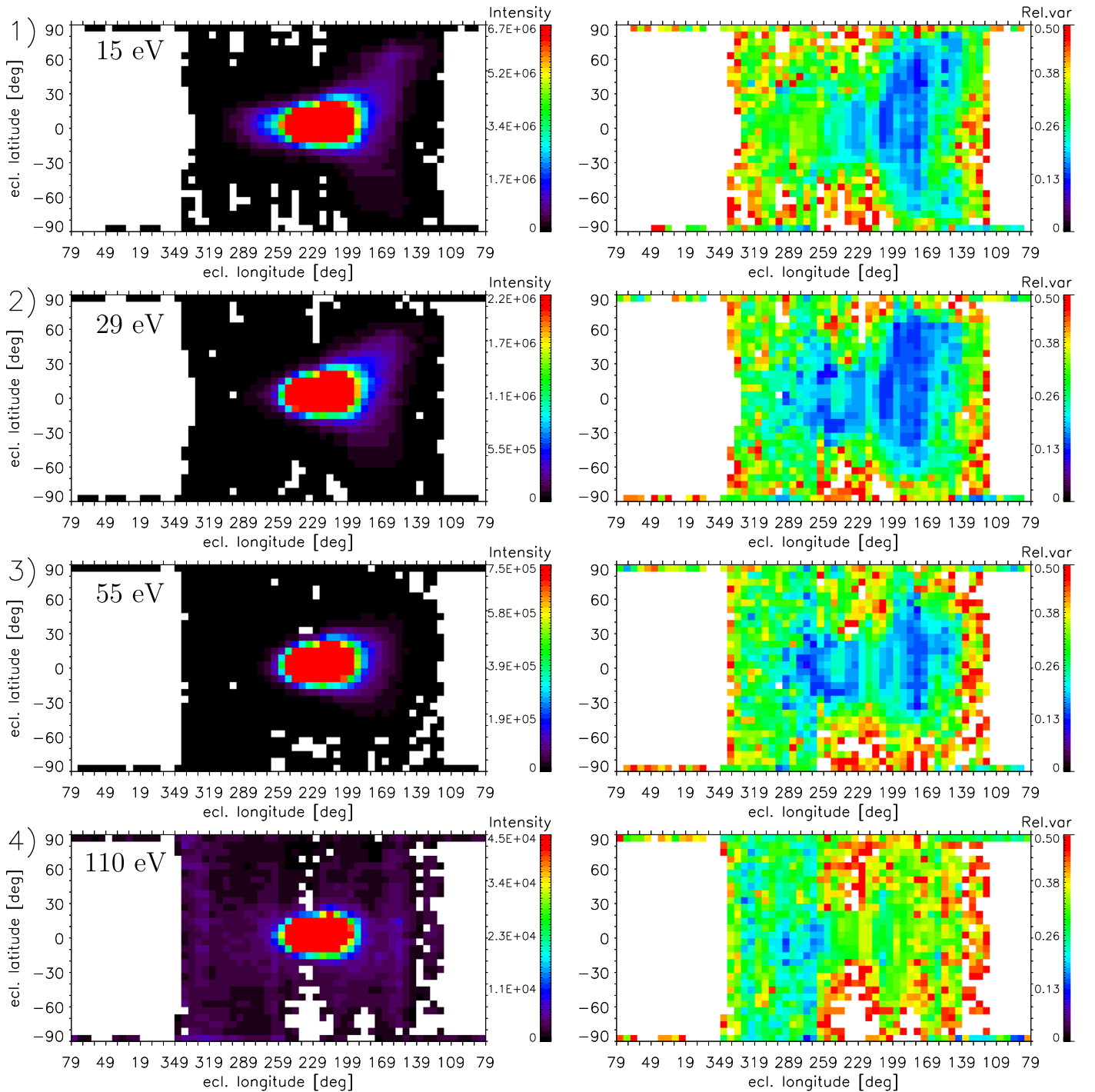
Figure 3. Intensity maps of the combined ISN and ENA signals, averaged over all 11 yr for energy bins 1–4 centered at 15, 29, 55, and 110 eV (top to bottom) in the spacecraft reference frame without correction for survival probability; ram observations only. The left column shows ENA and ISN intensities in units of cm^{-2} sr^{-1} s^{-1} keV^{-1}, the right column shows the relative variability (Equation (1)) over 11 yr.

ionization rates and radiation pressure (see Appendix C). The change in survival probabilities increased the derived ENA intensities by almost a factor of 2 (compare the green with the blue curve in Figure 7). Integrating over the full solar cycle increases also the ENA intensities at energies below 400 eV compared with the case for the first 4 yr of IBEX-Lo data depending on specific sky region (see Section 4.4).

Figure 7 illustrates these points by comparing the ENA energy spectrum for the Voyager 2 direction (black curve: all 11 yr, red curve: years 2009–2012) with the earlier energy

spectrum from Galli et al. (2016; dark green curve), and the energy spectrum in Fuselier et al. (2021) based on the algorithm by Galli et al. (2016) but including revised survival probabilities (orange curve). The blue curve shows the spectrum derived with the same algorithm and data used by Galli et al. (2016), but evaluated with the revised survival probabilities from the present paper, and the red curve shows the energy spectrum averaged over the years 2009–2012 instead of 2009–2019. These five sets of spectra indicate that the differences can be attributed to changes in the survival
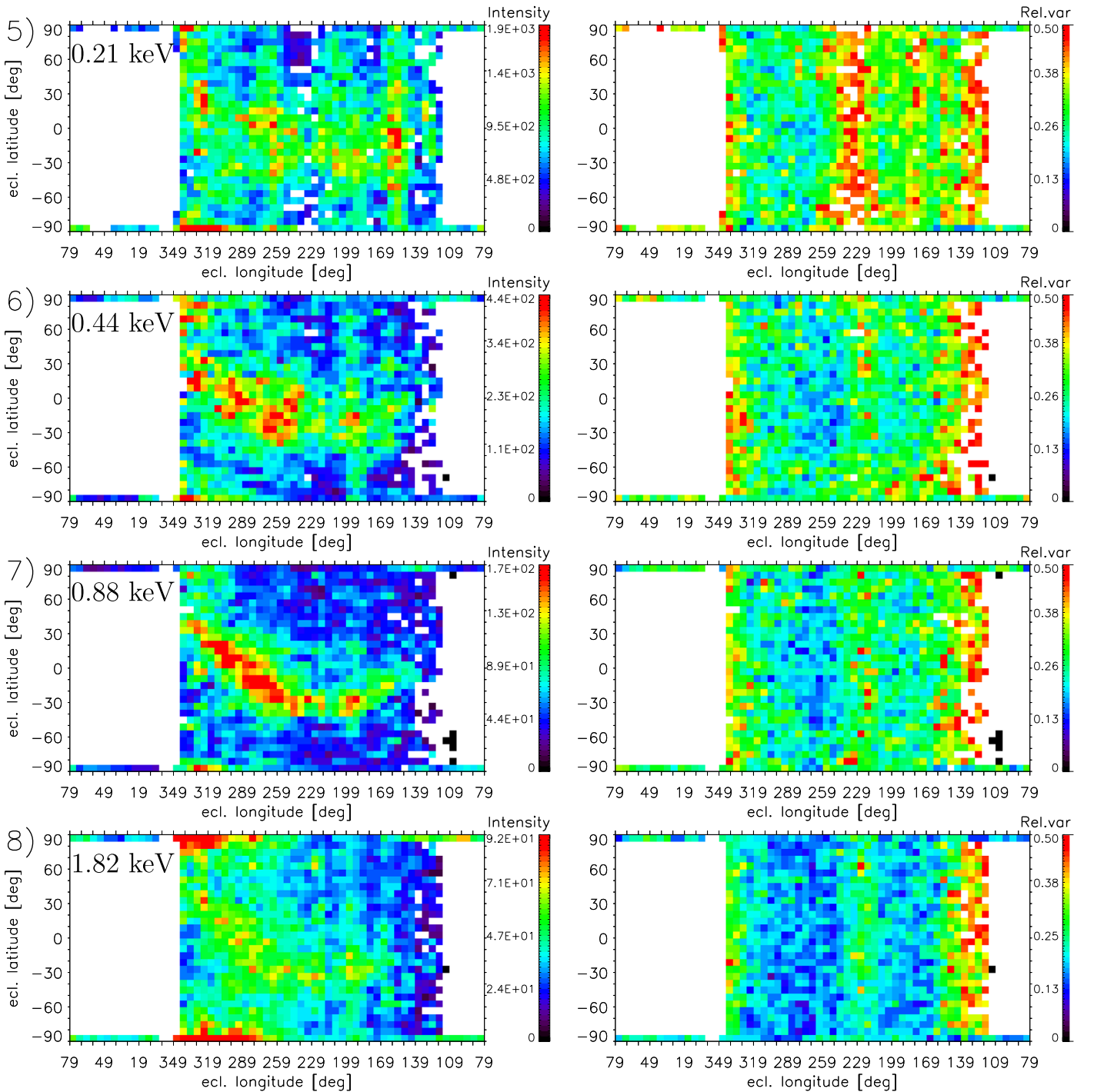
Figure 4. ENA intensity maps averaged over all 11 yr for energy bins 5–8 centered at 0.21, 0.44, 0.88, and 1.82 keV (top to bottom) in the spacecraft reference frame without correction for survival probability; ram observations only. The left column shows ENA intensities in units of cm^{-2} sr^{-1} s^{-1} keV^{-1}, the right column shows the relative variability (Equation (1)) over 11 yr.

probabilities and different time periods for averaging (see Section 4.4 to see why the time period may matter for 50–200 eV). In most cases, these differences are not significant with respect to the error bars. The relative error bars in this figure and the following figures of energy spectra from CG-SP-Ram and CG-SP-Antiram maps are 50% of the average intensity at energy bins 3 and 4 (50–100 eV) and 30% relative uncertainty for energy bins 5–8 (above 100 eV; Fuselier et al. 2014; Galli et al. 2014). These uncertainties include systematic uncertainties due to background sources and calibration and are usually

much larger than the temporal and spatial variability within a sky region over 11 yr. The agreement between the energy spectrum from earlier studies (Galli et al. 2016) with the present energy spectrum within the uncertainties serves as a cross-check of the analysis because they are based on two completely independent mapping algorithms.

Having compared and validated energy spectra from this data release with previous studies, we have to consider one more consistency test for the energy spectra, in particular at low energies where the ubiquitous background and other background sources
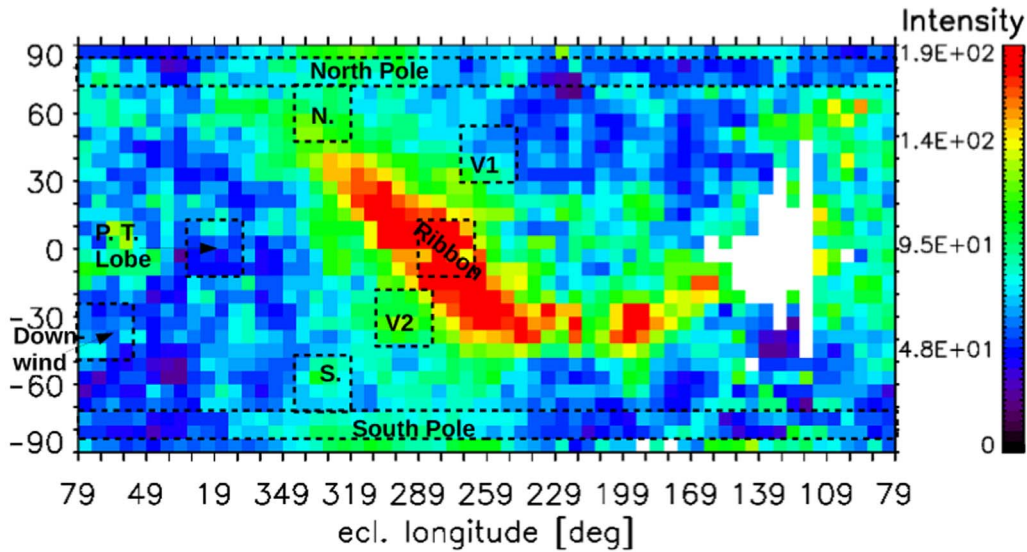
Figure 5. The nine sky regions selected for this study, plotted on an ENA intensity map of energy bin 7 averaged over all 11 yr, including Compton–Getting and ENA survival probability correction.

Table 3
Sky Regions Used for Energy Spectra and Year-by-year Variations

Name	Ecl. Long.	Ecl. Lat.	Ram or Antiram?	References to McComas et al. (2020)
South	318° ...342°	−72° ...−48°	both	
North	318° ...342°	48° ...72°	both	
South Pole	circumpolar	−72° ...−84°	both	South Pole
North Pole	circumpolar	72° ...84°	both	North Pole
Voyager 1	246° ...270°	30° ...54°	ram	Voyager 1
Voyager 2	282° ...306°	−42° ...−18°	ram	
Downwind	54° ...78°	−48° ...−24°	antiram	Central Tail
Port Tail Lobe	6° ...30°	−12° ...12°	antiram	Port Tail Lobe
Ribbon	264° ...288°	−12° ...12°	ram	

(such as the ISN) become more intense relative to the heliospheric ENA signal: energy spectra, corrected for Compton–Getting and survival probability, can be calculated from the maps both for ram and for antiram observations for the same region in the sky. If nonheliospheric sources dominate the retrieved energy spectrum, this would show up as a discrepancy between the ram and antiram energy spectra. The best sky regions for this test are the South and the North regions, which were covered both in ram and antiram maps in most years. Figure 8 shows this ram versus antiram comparison of energy spectra for the "North" sky region: The energy spectra agree within the estimated uncertainties down to an energy of roughly 50 eV. At the lowest energy bins, the discrepancy between ram and antiram observations becomes significant. Whereas the spectral shape is similar for both sets of observations, there is a tendency to have higher ENA intensities throughout the energy spectrum if antiram observations are included. This can be attributed to the antiram observations having a lower signal-to-background ratio, which tends to bias for higher average ENA intensities because of possible outliers being included in the average.

Based on Figure 8, we recommend to preferentially use the energy spectra derived from ram observations (CG-SP-Ram-Maps) unless a specific sky region was not covered by ram observations. Moreover, the ENA intensities derived for inertial energies below ∼50 eV for any region and for any map product should be interpreted only as upper limits. Unfortunately, the

downwind hemisphere from roughly 0° to 120° (including the macropixels Downwind and Port Tail Lobe) were only covered with antiram observations.

Figure 9 shows the energy spectrum of the derived ENA intensities for all sky regions covered with ram observations in the heliocentric frame at 100 au distance (CG-SP-Ram-Maps). The energy values for these energy spectra in the heliocentric frame are not the nominal central energies of IBEX-Lo but rather the shifted energies due to the Compton–Getting transformation, depending on the specific region in the sky. As we average over a macropixel, this introduces a spread in energy (20% relative uncertainty in the most extreme case for energy bin 2 for ram-only maps). This spread in energy is much smaller than the intrinsic bandwidth of the energy bins of $\Delta E/E = 0.7$. The shifted energy values are, to good approximation, constant over the 11 yr of averaging. The energy spectra overlap within the error bars for all regions down to roughly 50 eV energy (in the inertial frame). Below ∼50 eV, the differences between different sky regions in Figure 9 become larger than the error bars. Moreover, the ENA intensities from this study significantly exceed the values derived by Galli et al. (2016) below 50 eV (compare black and red versus green curves in Figure 7). They also exceed the upper limit of a few 10^4 cm^{-2} sr^{-1} s^{-1} keV^{-1} below 100 eV derived from Lyα observations (Wood et al. 2007). This suggests that there are likely still background sources at the lowest energies that could not be completely eliminated before the transformation to the inertial reference frame.
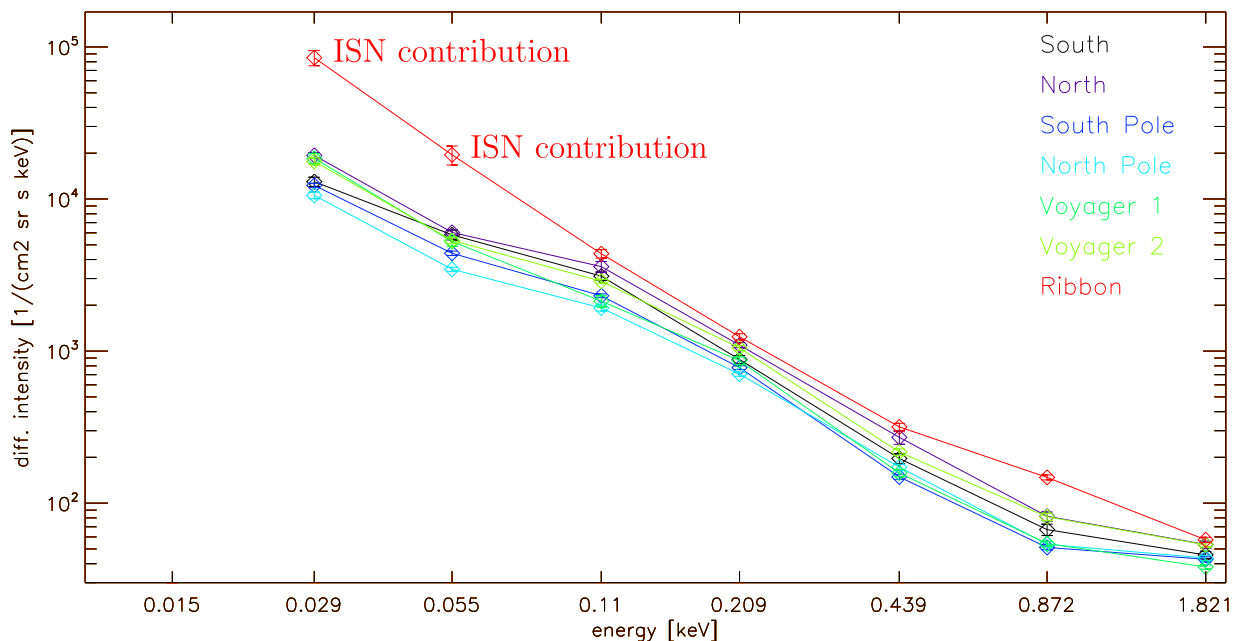
Figure 6. ENA energy spectra without Compton–Getting and ENA survival probability correction for all different viewing directions (colored labels) for the 11 yr average ENA intensities 2009–2019, ram observations only. The error bars depict only the statistical variabilities, the excess intensity at low energies in the Ribbon region is caused by ISN He and H.
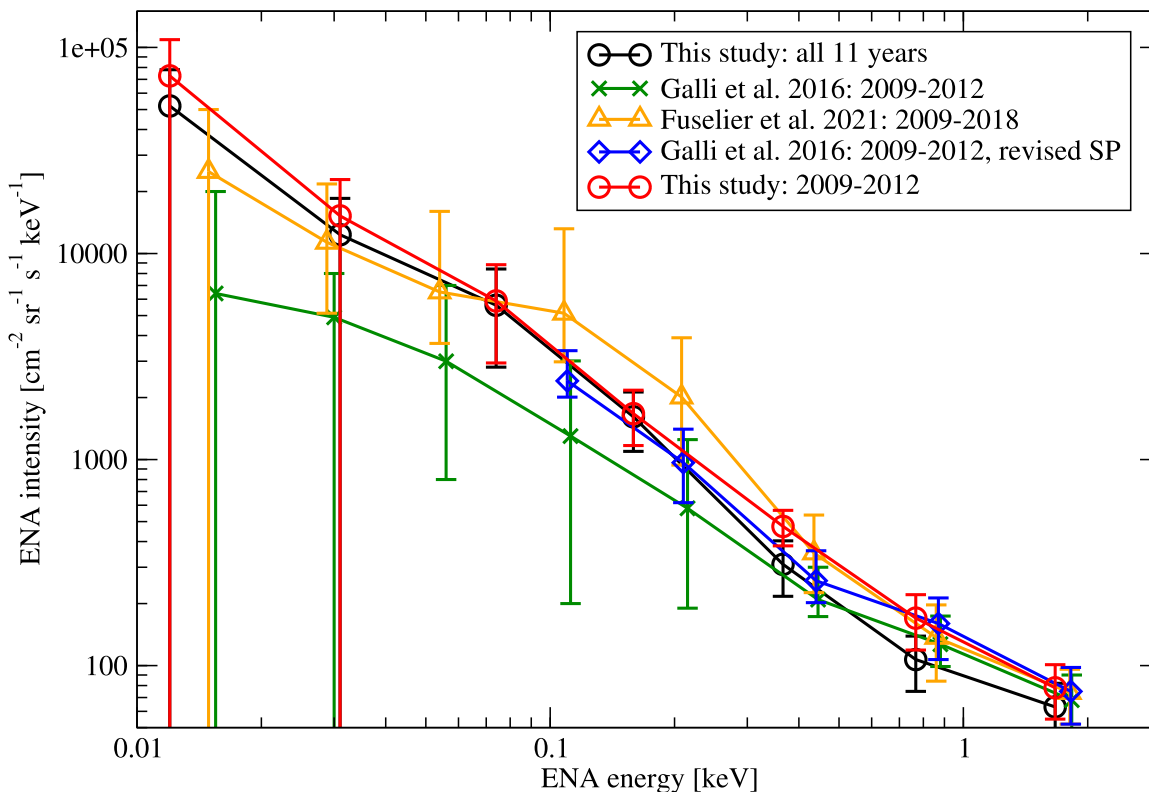

Figure 7. ENA energy spectra including Compton–Getting and ENA survival probability correction for the Voyager 2 direction, comparing this study to previous studies for a subset of years.

Relying on arithmetic means to generate energy spectra from a map region compared with using median values (Galli et al. 2016) also tends to bias for higher intensities, but this effect accounts for less than 20% relative change in the energy spectrum down to the lowest energies in Figure 7. An additional reason for the observed discrepancies below 50 eV might be statistics. Several sky regions

(e.g., South, North, Voyager 2, and the Ribbon region in Figure 9) have only 1–4 valid pixels to define the energy spectrum in energy bins 1, 2, and 3. All other pixels in the region are considered invalid because of insufficient exposure or too high interannual variability which can be caused by variable background sources or strong ISN signals varying with solar cycle. We provide three
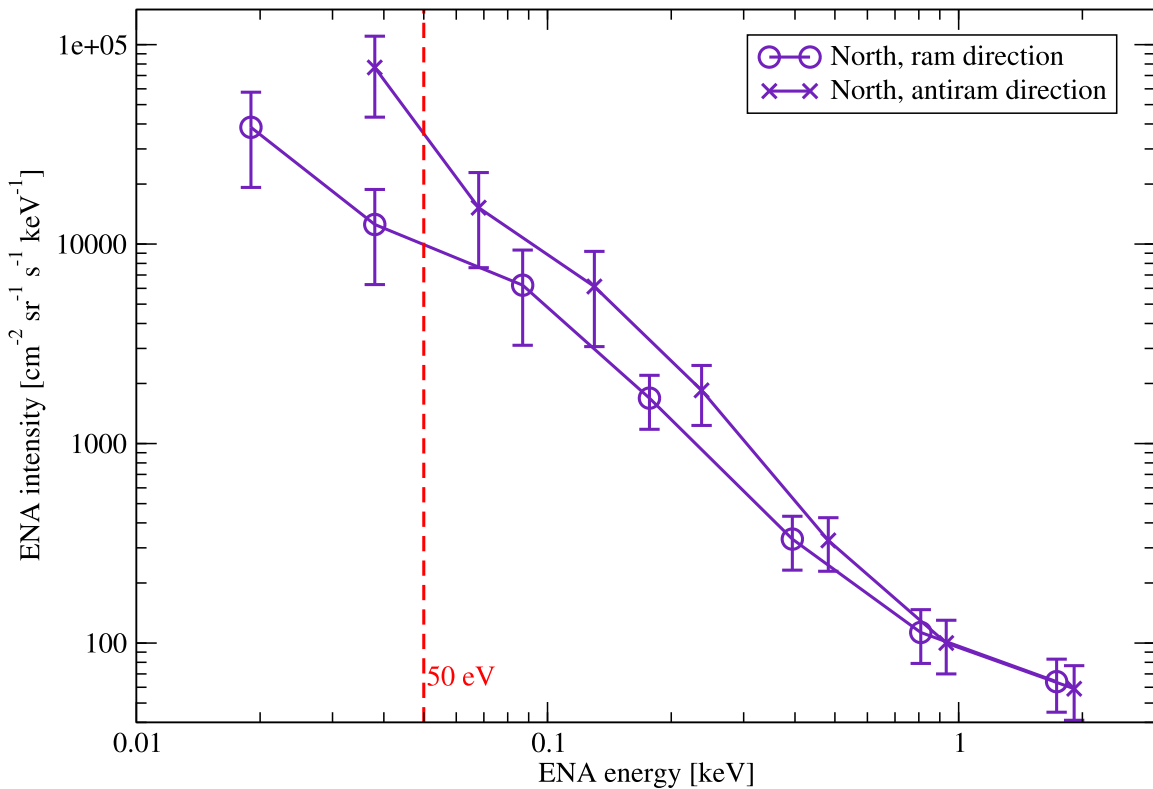
Figure 8. ENA energy spectra with Compton–Getting and ENA survival probability correction for the same sky region for ram observations (circles) and antiram observations ("X" symbols). The energy spectra should be the same if the background were completely eliminated.

tables of energy spectra. Table 4 lists the energy spectra for all seven sky regions covered by CG-SP-Ram-Maps averaged over all 11 yr (corresponding to the curves shown in Figure 9). Table 5 lists the energy spectra from the CG-SP-Ram-Maps, too, but averaged over all years of low solar activity (2009–2011 and 2017–2019). Finally, Table 6 lists the energy spectra from the CG-SP-Antiram-Maps for the two regions in the downwind hemisphere that were never covered by ram observations (Port Tail Lobe and Downwind) and for the North and South regions that also served as comparative case for Figure 8.

In summary, energy spectra from regions not strongly affected by the ISN inflow are reliable down to ENA energies of roughly 50 eV in the inertial reference frame. Preference is given to the ram-only maps and derived energy spectra because of the better signal-to-background ratio. The Ribbon is most pronounced at 0.9 keV and blends into the globally distributed flux between 100 and 200 eV, at least for the macropixel in the ecliptic plane (see Figure 9). Aside from the IBEX Ribbon, the heliospheric ENA distribution is homogeneous across the entire sky at low energies. The description "Globally Distributed ENA flux" first coined by McComas et al. (2009b) for these ENAs is apt. Most energy spectra observed with IBEX-Lo between 100 eV and 1 keV are approximated by a single power law, with the spectral index $\gamma = -1.9 \pm 0.1$ for North and Voyager 1 direction and -1.7 ± 0.1 for Voyager 2 direction (for the values in Table 4). The energy spectra start out significantly flatter below 100 eV ($\gamma > -1$ for North, South, and Voyager 2 regions), as seen both in the spacecraft reference frame (Figure 6) and in the inertial reference frame (Figure 9). This spectral flattening is made more pronounced by the transient ENA intensity increase around 200 eV during solar maximum seen across the sky (see next Section 4.4). This

time-dependent effect is also visible in Figure 7 for the Voyager 2 direction. For the subset of 2009–2012, no significant change in the spectral index throughout the IBEX-Lo energy spectrum (red line in Figure 7) shows up, whereas a hump in the spectrum appears if the 11 yr average is used instead (black line in same figure). However, Galli et al. (2016) already found, based on IBEX-Lo data from the years 2009–2012 only, a flattening or even a rollover around 100 eV for several regions. The flattening of the energy spectrum from 1 to 2 keV appears in most regions but seems to disagree with the IBEX-Hi energy spectra that show a steeper power law ($\gamma \leqslant -2$ for all ecliptic latitudes within $\pm 30°$ according to Figure 15 in McComas et al. 2020). The reason for the discrepancy between the IBEX-Lo and IBEX-Hi energy spectra observed between 1 and 2 keV is not understood so far. In this overlapping energy range, preference is given to the spectra derived with IBEX-Hi due to its better S/N. The spectral shape is a question that will be readdressed with the IMAP-Lo and IMAP-Hi imagers on the upcoming IMAP mission (McComas et al. 2018).

4.4. Temporal Evolution

Previous analyses of ENA intensities measured with IBEX-Lo showed no significant changes between individual years in solar wind energies between 0.4 and 2 keV (Fuselier et al. 2014; Galli et al. 2014, 2016; Reisenfeld et al. 2016; Galli et al. 2017). Galli et al. (2017) noted, however, that the ENA intensities measured in energy bins 4 and 5 (corresponding to roughly 0.1 and 0.2 keV) appeared to increase from 2009 onward and peaked in 2015. We now can revisit these time series for one complete solar cycle from 2009 to 2019.
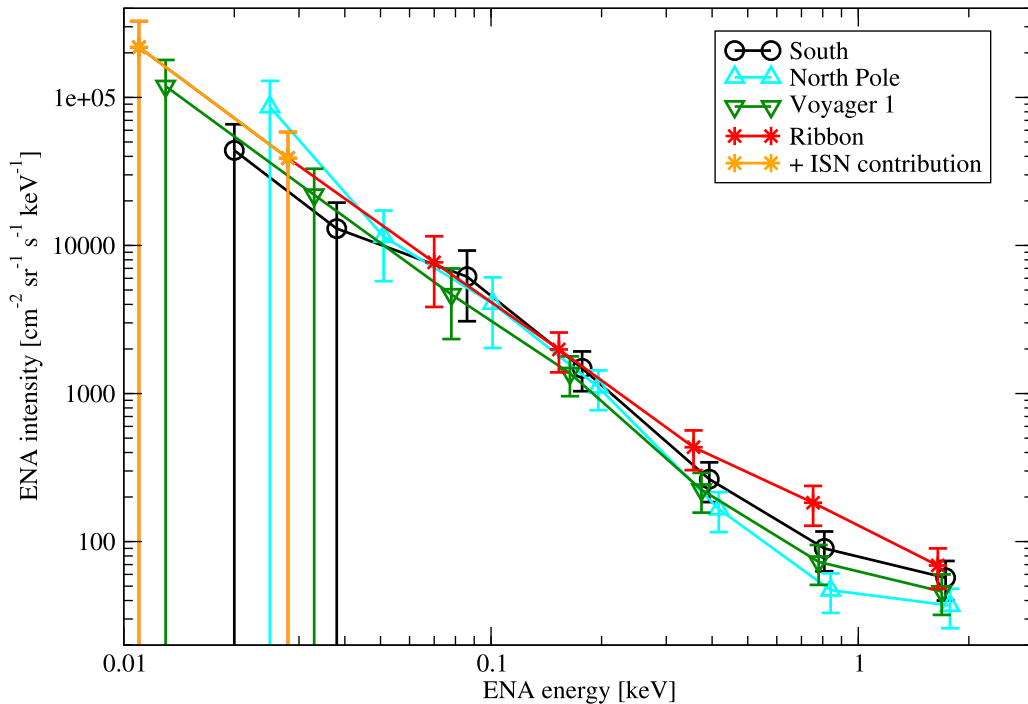
Figure 9. ENA energy spectra of CG-SP-Ram-Maps (Compton–Getting transformation and ENA survival probability included, ram observations only) for four different sky regions (black circles: South, cyan triangles up: North Pole, green triangles down: Voyager 1, red/orange asterisks: Ribbon) for the 11 yr average ENA intensities 2009–2019. The regions North, South Pole, and Voyager 2 were omitted from this plot for the sake of readability; they would overlap within the uncertainties with the spectra for South, North Pole, and Voyager 1, respectively.

Figure 10 shows the time series of ENA intensities in analogy to Figure 26 from McComas et al. (2020) for the different sky regions covered in ram direction for all 8 IBEX-Lo energy bins. These time series are based on the annual energy spectra of the SC-Ram-Maps using exposure weights >200 to exclude undersampled regions. For these time series, the exact energy is irrelevant as long as we compare the same sky region. The years 2016 and 2019 had poor coverage for several spectral entries (see Figure 1) and thus were omitted from these time series. The black curves with asterisks in the South Pole and North Pole panels show the corresponding time series for the identical regions for the IBEX-Hi energy bin centered at 1.1 keV (McComas et al. 2020). The bottom right panel shows the monthly averaged sunspot numbers (SILSO, World Data Center 2008) as a proxy for the activity over the solar cycle. The time tags on all x-axes indicate the first of January of each calendar year.

Figure 11 shows the time series in analogy to Figure 10 for CG-SP-Ram maps and Figure 12 shows the three time series with sufficient coverage for the the CG-SP-Antiram maps. For reference, the orbit-by-orbit average of the background counts observed with the IBEX background monitor are shown in the bottom right panels. These background monitor time series correlate well with the solar activity in the bottom right panel of Figure 10. The time range corresponding to the year 2015 in ENA maps is highlighted in red. The lowest energy bin had to be omitted from these time series because of the large uncertainties introduced by the Compton–Getting and survival probability correction at the lowest energies. Also note that the actual energies depend on the selected sky region in these two figures.

The discussion of potential temporal evolution in ENA intensities over the solar cycle can be organized into low, intermediate, and high energies. The time series in the two lowest energy bins 1 and 2, below 50 eV, may be affected by nonheliospheric background sources, as we have shown in the previous section (see Figure 8). Obvious cases are the time series of 15 and 29 eV for the Ribbon region (red and orange curves in the bottom left panel of Figure 10). Their fall and rise with the solar cycle is caused by the ISN He and H inflow at these energies and direction.

At energies above 200 eV (the bluish time series for energy bins 6, 7, and 8), the ENA intensities in most regions dropped around 2011 or 2012 and from then onward showed moderate variation until 2019. The intensities recovered by 2019 to the 2009 levels for some, but not for all sky regions. One region where the ENA intensity has not returned yet to its initial level is the Ribbon (bottom left panel in Figures 10 and 11). This evolution of ENA intensities at solar wind energies agrees with the IBEX-Hi measurements, in particular for the Ribbon case (McComas et al. 2020). However, the drop seen with IBEX-Lo is more pronounced than that seen in the IBEX-Hi time series (compare dark blue and light blue curves with black curves for 1.1 keV in the North Pole and South Pole regions in Figure 10).

The most prominent feature in virtually all sky regions, in the spacecraft and inertial reference frames and for ram and antiram observations, is the strong rise and fall in ENA intensities between 50 and 200 eV around the year 2015. These are the green peaks in Figures 10–12. This trend of rising ENA intensities at 100 and 200 eV was already observed by Galli et al. (2017), but now it can be tracked over the full solar cycle. The explanation for this rise and fall in ENA intensities is not known yet. As this signal is robust against reference frame transformations and is very specific for a few adjacent energies, an instrument-related effect is highly unlikely. As the trend looks similar in bins 4 and 5, whereas it is weaker in energy bin 3 and usually does not occur in energy bins 1 and 2, it cannot be attributed to ISN He or H. In principle, the ENA rise and fall could be partially due to higher background from local electrons or similar local contamination during the solar

Table 4
Table of the Energy Spectra Derived from CG-SP-Ram-Maps for all 11 yr, Corresponding to the Curves in Figure 9

E	So	E	No	E	SP	E	NP	E	V1	E	V2	E	Ri
0.020	**43,878**	**0.019**	**38,478**	**0.025**	**82,640**	**0.025**	**86,257**	**0.013**	**119,018**	**0.012**	**52,011**	**0.011**	**218,359**
0.038	**12,993**	**0.038**	**12,532**	0.051	16,752	0.051	11,481	**0.033**	**21,970**	**0.031**	**12,344**	**0.028**	**38,918**
0.086	6162	0.087	6221	0.101	4879	0.101	4062	0.078	4666	0.074	5608	0.070	7690
0.177	1481	0.177	1689	0.196	1319	0.196	1103	0.164	1372	0.159	1612	0.153	1986
0.393	264	0.394	332	0.417	149	0.417	166	0.374	224	0.366	310	0.356	434
0.808	90	0.809	113	0.841	45	0.841	47	0.780	73	0.767	107	0.753	183
1.729	57	1.731	64	1.776	36	1.777	37	1.687	46	1.668	63	1.646	69

Note. Energies "E" are stated in units of keV, ENA intensities are given in units of $cm^{-2}\ sr^{-1}\ s^{-1}\ keV^{-1}$ for the sky regions "So" = South, "No" = North, "NP" = North Pole, "SP" = South Pole, "V1" = Voyager 1, "V2" = Voyager 2, and "Ri" = Ribbon between Voyager 1 and Voyager 2. Uncertainties of ENA intensities: 30% for energies above 0.1 keV, 50% between 0.05 and 0.1 keV, entries below 50 eV printed in bold are upper limits.

Table 5
Table of the CG-SP-Ram-Maps Energy Spectra for the Years of Low Solar Activity (2009–2011 and 2017–2019)

E	So	E	No	E	SP	E	NP	E	V1	E	V2
0.020	**32,442**	**0.019**	**42,067**	**0.025**	**61,830**	**0.025**	**92,608**	**0.013**	**123,256**	**0.012**	**55,544**
0.038	**11,116**	**0.038**	**9655**	0.051	12,268	0.051	11,727	**0.033**	**21,790**	**0.031**	**11,691**
0.086	5075	0.087	6684	0.101	5453	0.101	5125	0.078	4885	0.074	4247
0.177	1246	0.177	1355	0.196	1110	0.196	1162	0.164	1139	0.159	1200
0.393	187	0.394	335	0.417	235	0.417	247	0.374	265	0.366	348
0.808	91	0.809	124	0.841	65	0.841	74	0.780	81	0.767	135
1.729	60	1.731	63	1.776	48	1.777	51	1.687	46	1.668	68

Note. Energies "E" are stated in units of keV, ENA intensities are given in units of $cm^{-2}\ sr^{-1}\ s^{-1}\ keV^{-1}$ for the sky regions "So" = South, "No" = North, "NP" = North Pole, "SP" = South Pole, "V1" = Voyager 1, and "V2" = Voyager 2. Uncertainties of ENA intensities: 30% for energies above 0.1 keV, 50% between 0.05 and 0.1 keV, entries below 50 eV printed in bold are upper limits.

maximum. However, the actual ENA rise appears nowhere before 2014, i.e., several years after the solar activity has reached maximum levels in 2012 (see bottom right panel in Figure 10). The fact that the rise and fall toward the North and the South are also observed in corrected antiram observations during the same years (see Figure 12) argues against a local source of the ENA rise and fall. The bottom panel in that figure hints at the ENA rise being delayed to 2018 or later for a sky region toward the downwind hemisphere in contrast to the maximum ENA intensity observed in 2015 for all sky regions toward the upwind or to the flanks. Unfortunately, the spatial coverage of the downwind hemisphere in later years is insufficient to reach a more firm statement here. The observed ENA wave is restricted to one or two years at most (2014 and in particular 2015) for most sky regions with the exception of the North and North Pole regions; in 2016 the ENA intensities drop back to 2009 levels again with the exceptions of the North and North Pole regions. The relative increase observed in 2015 exceeds a factor of two for most regions, but the actual value varies strongly between different regions: a relative enhancement by a factor of 9 for Voyager 1, a factor of 5 for South Pole, and a factor of 2.4 for the Ribbon macropixel according to Figure 11. The only geographical pattern that appears seems to be that the ENA rise is less severe but extends over several years for the North and North Pole regions whereas it is strong and rapid (max. 2 yr) for all other regions.

5. Discussion

This paper and the associated data release provide the heliosphere community with a comprehensive set of model-free ENA data. We therefore do not include detailed model-based interpretations of the data presented here. The ENA intensity maps in the spacecraft reference frame without survival probability

Table 6
Table of the CG-SP-Antiram-Maps Energy Spectra for all 11 yr

E	South	E	North	E	Downwind	E	Lobe
0.038	**80,062**	**0.038**	**76,774**	**0.048**	**46,639**	**0.057**	**65,541**
0.068	19,263	0.068	15,226	0.082	10,396	0.091	12,898
0.130	5759	0.130	6128	0.147	3616	0.159	5457
0.237	1870	0.237	1849	0.260	1133	0.275	1575
0.482	253	0.482	327	0.512	168	0.533	207
0.933	76	0.933	100	0.975	60	1.003	54
1.909	52	1.910	59	1.968	45	2.008	40

Note. Energies "E" are stated in units of keV, ENA intensities are given in units of $cm^{-2}\ sr^{-1}\ s^{-1}\ keV^{-1}$ for the sky regions South, North, Downwind, and Port Tail Lobe. Uncertainties of ENA intensities: 30% for energies above 0.1 keV, 50% between ∼0.05 and 0.1 keV, entries printed in bold are upper limits.

correction will serve as reference for future modeling efforts to reproduce these measurements. Nevertheless, the two main open questions raised by these 11 yr IBEX-Lo maps should be pointed out. These questions concern the absolute ENA intensity exceeding most model predictions and the strong rise and fall of ENAs at 50–200 eV energy around the year 2015.

Even before this more comprehensive data release, studies found a factor of 2–10 underestimation of ENA model predictions compared with IBEX-Lo and IBEX-Hi observations at all energies considered (Kornbleuth et al. 2021; Fuselier et al. 2021). The results below 0.5 keV from the present study imply an underestimation of an order of magnitude (similar to Fuselier et al. 2021). The ENA wave at 50–200 eV, which was not or only partially included in the previous IBEX-Lo studies by Galli et al. (2016, 2017), increased this discrepancy. However this discrepancy
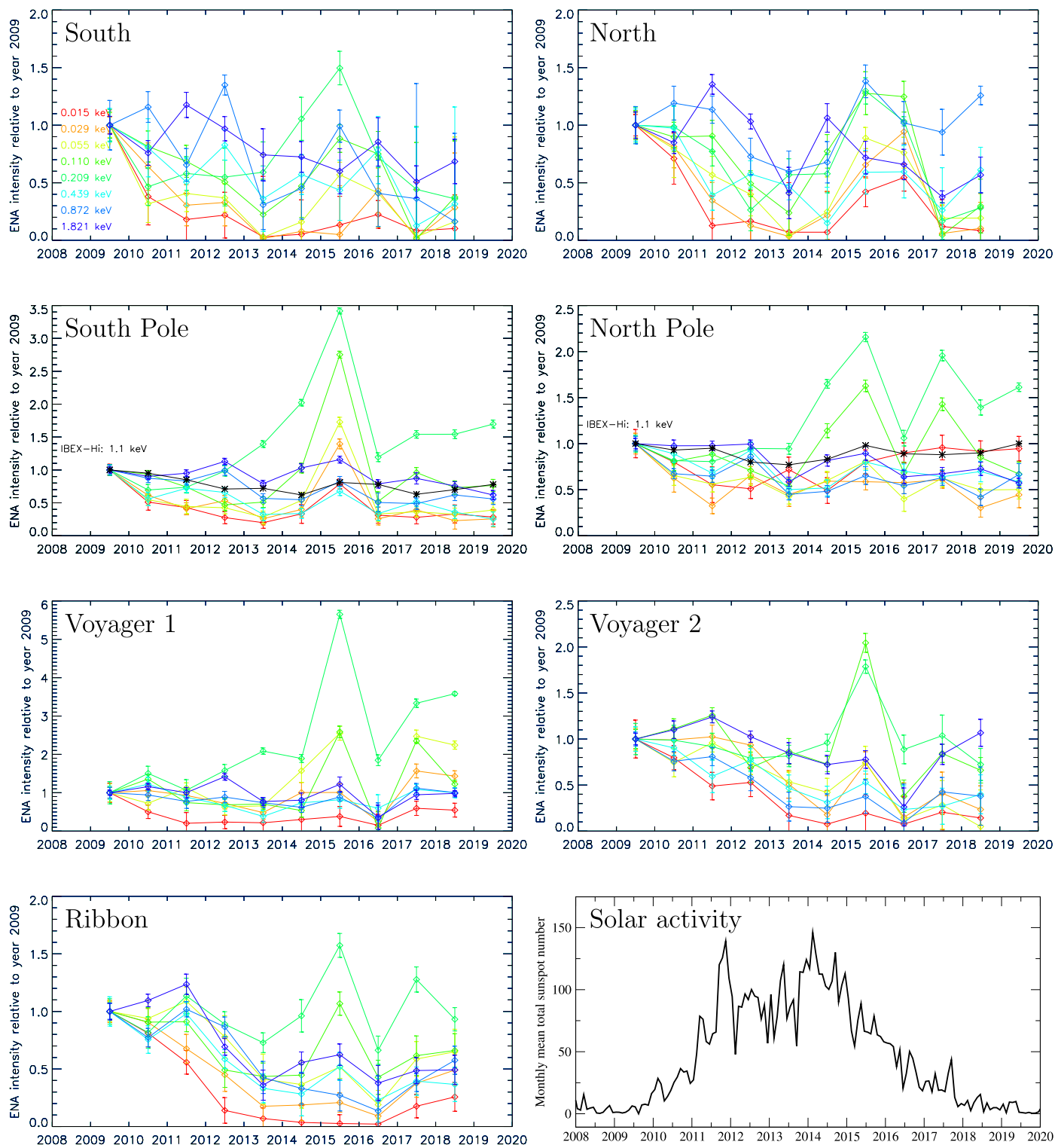
Figure 10. Temporal evolution of ENA intensities for the seven regions covered with ram observations, no correction for Compton–Getting or survival probability. The eight energy bins are color coded from red (15 eV) to blue (1.8 keV), and all ENA intensities are normalized to the one measured in the first year (2009). The black curves in South Pole and North Pole regions show the IBEX-Hi time series measured at 1.1 keV (McComas et al. 2020). The bottom right panel shows the monthly sunspot numbers (SILSO, World Data Center 2008).

still is an order of magnitude larger for energies between 0.1 and 0.5 keV (compared to the ENA model used by Fuselier et al. 2021) if we average the observed ENA energy spectrum only over the years of low solar activity (see Table 5) or over the first 4 yr of IBEX observations (see red energy spectrum in Figure 7). The

IBEX-Lo instrument background cannot explain this discrepancy. For instance, the change in the PAC high voltage in 2012 was corrected for, and the ENA intensities around the solar minima before and after this change are similar. Moreover, the heliospheric ENA intensities observed with IBEX-Hi and IBEX-Lo agree at the

Figure 11. Temporal evolution of ENA intensities for the seven regions covered with ram observations, corrected for Compton–Getting and survival probability. The energy bins are color coded from orange (around 20 eV) to blue (around 1.7 keV), and all ENA intensities are normalized to the ENA intensity measured in the first year (2009). The bottom right panel shows the orbit-by-orbit average of the IBEX background monitor.

solar wind energy (1 keV) in absolute terms. Thus the underestimation of ENA model predictions cannot be attributed to one instrument alone. A factor of 2 of discrepancy between observed and predicted ENA intensities can be explained by the hydrogen density at the termination shock being 40% higher than assumed in previous models (Swaczyna et al. 2020). In addition, this increased

neutral hydrogen density may imply a different ionization degree and a different total density of interstellar matter in front of the heliosphere. If true, the plasma flow, plasma heating, and production of pickup ions in the inner heliosheath also have to be modified substantially to allow for more accurate ENA model predictions. Assuming the observed ENA intensities exceed the
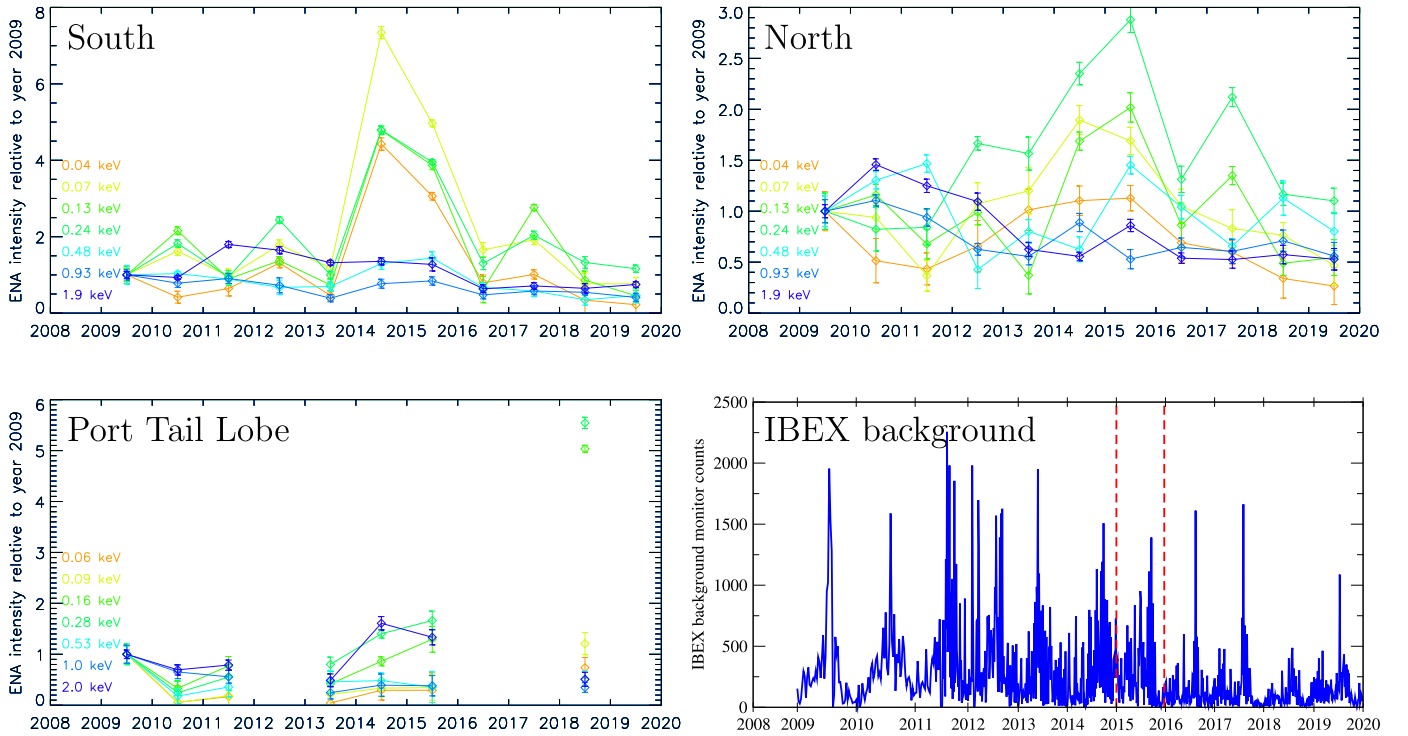
Figure 12. Temporal evolution of ENA intensities for the three regions covered with antiram observations with the best statistics, corrected for Compton–Getting and survival probability. The energy bins are color coded from orange (roughly 40 eV) to blue (around 2 keV), and all ENA intensities are normalized to the ENA intensity measured in the first year (2009). The bottom right panel shows the orbit-by-orbit average of the IBEX background monitor.

intensities predicted from pickup ions in the inner heliosheath by a factor of 5–10, one implication could also be that a part of the observed ENAs (in particular below 500 eV) are secondary ENAs from beyond the heliopause. This question must be investigated in future studies.

From the spatial distribution of observed ENAs we learn that they are indeed, with the exception of the Ribbon, a "globally distributed flux"; they are rather uniformly distributed across all sky regions including the downwind hemisphere, which precludes secondary hydrogen ISN from being a major contribution to the low-energy ENA maps and spectra presented here (Swaczyna et al. 2018). Attributing these ENAs to a region of origin is important because this directly affects how derived pressure times line-of-sight maps derived from these ENA intensities are interpreted. If a large fraction of these ENAs originate from outside the heliopause their parent ions do not contribute to the plasma pressure in the inner heliosheath. In this case the parent ions would contribute to the interstellar side of the pressure balance, and the measured ENA intensity cannot be transformed directly into heliosheath thickness times heliosheath pressure.

The second open question concerns the transient ENA rise at 50–200 eV in most sky regions around 2015. Sokół et al. (2021) found that repeating pulses (10.2 yr) of the solar wind pressure can cause periodic solar cycle variations of the ENA production in the heliosheath and that these variations showed up in IBEX-Hi data at energies from 0.7 to 4.3 keV with a delay of 2–5 yr between the solar wind pulse and observed ENA response. The delay time or trace-back time (Zirnstein et al. 2018a; Reisenfeld et al. 2021) describes the time it takes the solar wind to travel from 1 au to the termination shock or beyond plus the time for the subsequently created ENA to travel back to 1 au to IBEX. This time obviously is a function

of the ENA energy in question. A 200 eV heliospheric ENA (the energy most markedly increasing and decreasing with solar cycle according to Figure 10) has a trace-back time of 10.4 yr, i.e., about one solar cycle. For this estimate, a magnetosonic speed in the heliosheath $v_{ms} = 314$ km s^{-1}, an average termination shock distance $d_{TS} = 100$ au and a heliosheath thickness $l_{HS} = 200$ au were assumed in the following equation (Zirnstein et al. 2018a; Reisenfeld et al. 2021):

$$t_b(E) = \frac{d_{TS}}{v_{SW}} + \frac{3}{2}\frac{l_{HS}}{v_{ms}} + \frac{d_{TS} + l_{HS}/2}{v_{ENA}(E)}. \quad (2)$$

The trace-back time indicates that for these ENAs of a few 100 eV we cannot tell from time alone if the observed increase in ENA intensities during solar maximum 24 is foreground (e.g., caused by higher fluxes of electrons) or if it is the result of processes in the heliosheath triggered by solar wind released around the previous solar maximum 23 (see Figure 13, the thick black line indicates a rolling average). As we see a similar temporal behavior of ENA intensities for polar and other sky regions, either the heliosheath thickness would be similar in different heliospheric directions or these observed ENA changes around 200 eV do not originate from plasma in the middle of the heliosheath. It is unclear if the quantitative differences in the ENA time series between the Northern and Southern hemispheres (see Figure 11) could be linked to asymmetries seen in solar wind speed data in the previous solar cycle (Tokumaru et al. 2015; Porowski et al. 2022).

There are at least three possible correlations between the rise and fall of ENA intensities around the year 2015 and the solar wind dynamic pressure measured at 1 au (see Figure 13). First, based on the trace-back time of roughly 10 yr for heliosheath ENAs, the observed rise and fall in ENAs around 2015 could be
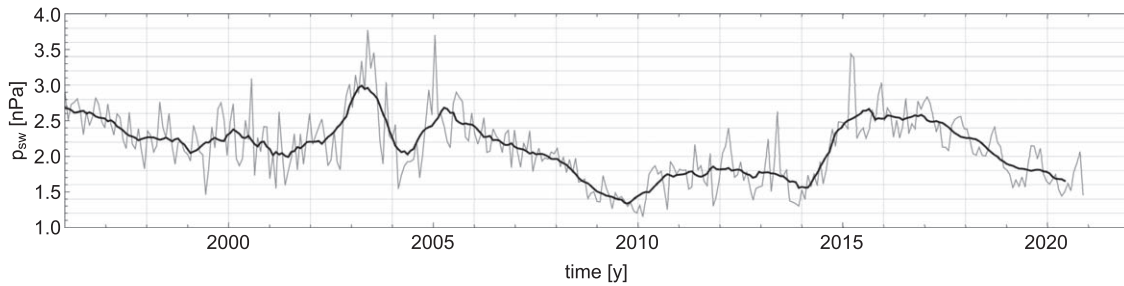
Figure 13. Solar wind dynamic pressure measured at 1 au from 1996 to 2020. The thick black line is a moving average over 13 Carrington rotations, and the thin gray line illustrates the Carrington rotation average time series based on the solar wind measurements collected by OMNI. Figure adapted from Sokół et al. (2021).
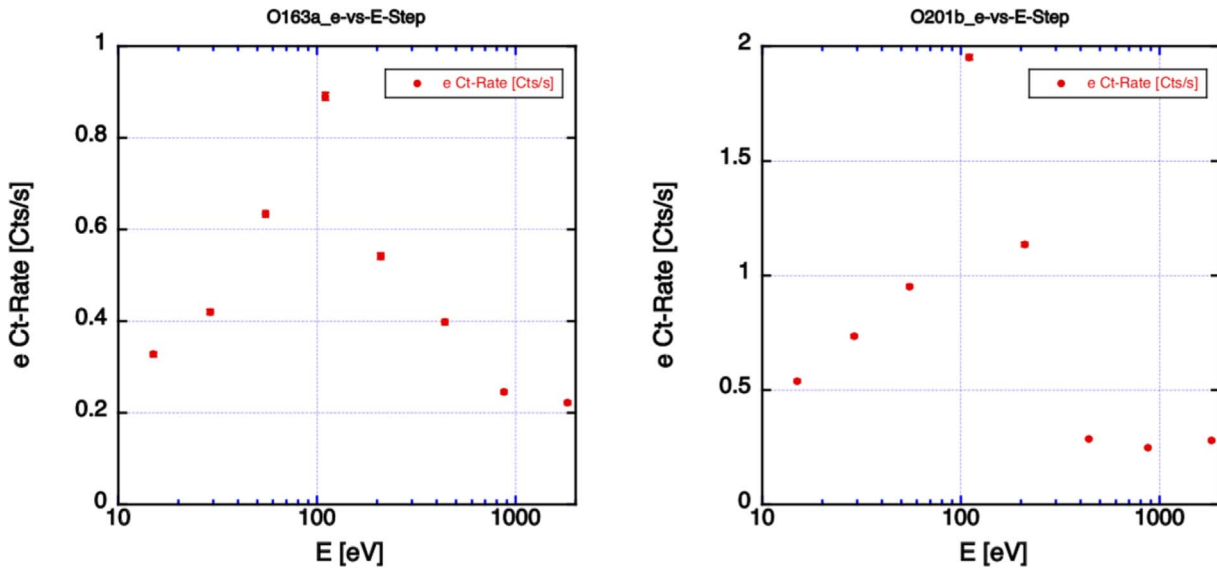

Figure 14. Electron count rates seen in the eight energy bins of IBEX-Lo over all spin angles for two orbits 163a (left panel) and 201b (right panel).

the product of the solar wind pressure pulses traveling outward in solar cycle 23 in 2003 and 2005 (see Figure 13). Second, the average dynamic pressure also increased in early 2015 when the ENA intensities increased. However, the mechanism of how a local increase in solar wind pressure could cause an immediate enhancement of ENAs in IBEX-Lo in a very restricted energy range is unknown. Individual coronal mass ejections passing Earth during the months of high solar wind dynamic pressure in 2015 do not seem to be related to the observed ENA intensities. The ENA intensities in energy bin 5 were high (the bright stripes at ecliptic longitudes from 180° to 270° in the first column and seventh row of Figure 1 correspond to January 1–March 15) well before the first super geomagnetic storm of solar cycle 24 (related to a coronal mass ejection passing Earth and IBEX on 2015 March 17 (Wu et al. 2016)). Finally, another remote ENA source could be corotating interaction regions propagating out to the termination shock where they produce an excess of low-energy ENAs. The trace-back time for 200 eV ENAs would calculate to 3–4 yr if they are created from solar wind interactions near the termination shock, i.e., if the l_{HS} terms in Equation (2) becomes negligible. This is interesting because the occurrence of corotating interaction regions started to increase with solar activity by the end of 2011, i.e., roughly 3 yr before the observed ENA rise. However, to corroborate any of these three hypotheses, future studies are needed to investigate if the proposed processes could produce the observed ENA intensities.

We also considered if the ENA rise and fall around 2015 could be caused by a local background. If the local electron background around IBEX was excessive in 2015 compared to all other years, the observed rise and fall of H⁻ count rates could be related to the higher sensitivity of IBEX-Lo energy bins 3–5 to electrons via TOF3 count rates as illustrated in Figure 14. However, if this hypothesis were true the ENA intensities in energy bin 4, independent of the transformed energy, should be by far the highest (see peak position in Figure 14). This disagrees with the observed time series in the spacecraft reference frame (Figure 10) and inertial reference frame (Figure 11) where energy bin 5 shows a much stronger relative rise compared to energy bin 4 for all sky regions except for the Voyager 2 region. Additional checks in a future study should include verification if IBEX-Lo TOF distributions in 2015 were markedly different than neighboring years and comparison of the quadrant distribution of TOF3 counts for 2015 versus other years. However, a general argument against a local background is that neither the solar activity nor the IBEX background monitor indicate that the year 2015 was particularly noisy compared to earlier years during high solar activity when the observed ENA intensities at 50–200 eV were much lower.

A local source in the spacecraft or Earth environment could in principle cause a transient increase in H⁻ count rates in IBEX-Lo, e.g., by pickup protons from the extended geocorona

(local H$^+$ densities $\sim 10^{-3}$ cm^{-3} at 20–30 Earth radii distance from Earth according to Gomez et al. (2021)). However, it is unclear why this signal would be restricted to the years around 2015, whereas the orbital configuration of IBEX has remained identical from 2011 onward, and why it would be restricted to 50–200 eV energies. Moreover, if the signal causing the ENA increase were local, i.e., comoving with the Earth and the spacecraft, it should appear much more pronounced for antiram observations than for ram observations at these low energies after the CG and SP corrections, which transform the signal to the inertial reference frame. In this respect, the South region may be suspicious whereas the signal looks very similar in the North in CG-SP-Ram (Figure 11) and CG-SP-Antiram time series (Figure 12). On the other hand, the ENA increase measured in energy bins 5 and 4 probably does not affect previous or future ISN studies, as only data from energy bins 1–3 are usually used to track ISN H and He (Swaczyna et al. 2022).

6. Conclusions

In this study, we have compiled and presented the heliospheric ENA data products from all IBEX-Lo observations for one solar cycle from 2009 until 2019. The main data products are the ENA maps in the spacecraft reference frame plus the derived energy spectra and time series of ENA intensities. Energy spectra in the inertial reference frame will be of particular importance for future investigations that compare ENA observations with model predictions to better constrain heliosphere models. Investigating different regions and post-processing steps we have come to the conclusion that the energy spectra in the inertial reference frame are reliable within the stated uncertainties down to 50 eV energy. Below that, the derived values should only be interpreted as upper limits. The ENA time series over the 11 yr can be categorized in three different timelines for very low energies (variation dominated by ISN signals), intermediate energies at 50–200 eV (strong rise and fall in most directions around 2015), and the solar wind energy at 0.4–2 keV (rather moderate variations in agreement with IBEX-Hi).

The low-energy ENA observations presented here have raised two main questions that remain open at present. The observed ENA intensity exceeds model predictions, in particular below 500 eV, and the production mechanism (a local source or a real heliospheric signal) behind the strong rise and fall of ENAs at 50–200 eV energy around the year 2015 remains unknown. These questions have to be investigated in more detail as IBEX-Lo continues to expand the measurements over more years. IBEX-Lo will remain operational until at least 2025 or longer to give a continuous time series of low-energy ENA observations over much more than one solar cycle and to bridge the gap until the arrival of IMAP (McComas et al. 2018).

Appendix A
Comparison of Mapping Methods

Here we briefly discuss the following comparisons and explain why we chose the following combination as the best method for IBEX-Lo heliospheric ENA maps in Section 4: histogram binning mode (HB) data instead of direct event data, "Super Good Times" instead of "Super Better Times", and ram versus antiram observations.

1. Clear preference is given to histogram over direct event ENA intensity maps because the throttling limitation of direct event data with respect to histogram data changes with time and signal strength, which makes correction difficult. An average correction factor therefore has to be applied to direct event data, which may result in an overestimation or underestimation for individual pixels compared to the more accurate HB data. The shortcomings of the direct event data are illustrated in Figure 15 for the ISN signal observed in energy bin 1 in the year 2009. Also at higher energies, poorer statistics introduced by direct event data compared to HB are another argument for histogram data.

2. "Super Good Times" lists are preferred over the "Super Better Times" lists: The decrease in statistics due to the additional TOF2 count rate criterion leads to an unacceptable increase in the S/N and signal-to-background ratio. This is illustrated in Figure 16. The right panel (based on "Super Better Times") shows a higher pixel-to-pixel variability; in particular individual pixels with excessively high ENA intensity become more numerous than for "Super Good Times".

3. Ram and antiram observations: Including antiram observations allows us to cover the full sky but may introduce additional background and escalate uncertainties below solar wind energies due to survival probabilities and Compton–Getting transformation. For spacecraft-centered maps, inclusion of antiram observations seems to be beneficial, as shown in Figure 17 for the year 2014, with the worst S/N. Full sky coverage is achieved instead of missing one third of the sky between 0°...120°, and the statistics of doubly covered pixels are better. However, to interpret the ENA intensity maps (and derived quantities such as the energy spectra) in a physically meaningful way preference is given to ram maps (CG-SP-Ram-Maps) if the sky region in question has been covered by ram observations (see Section 4.3 for more details).
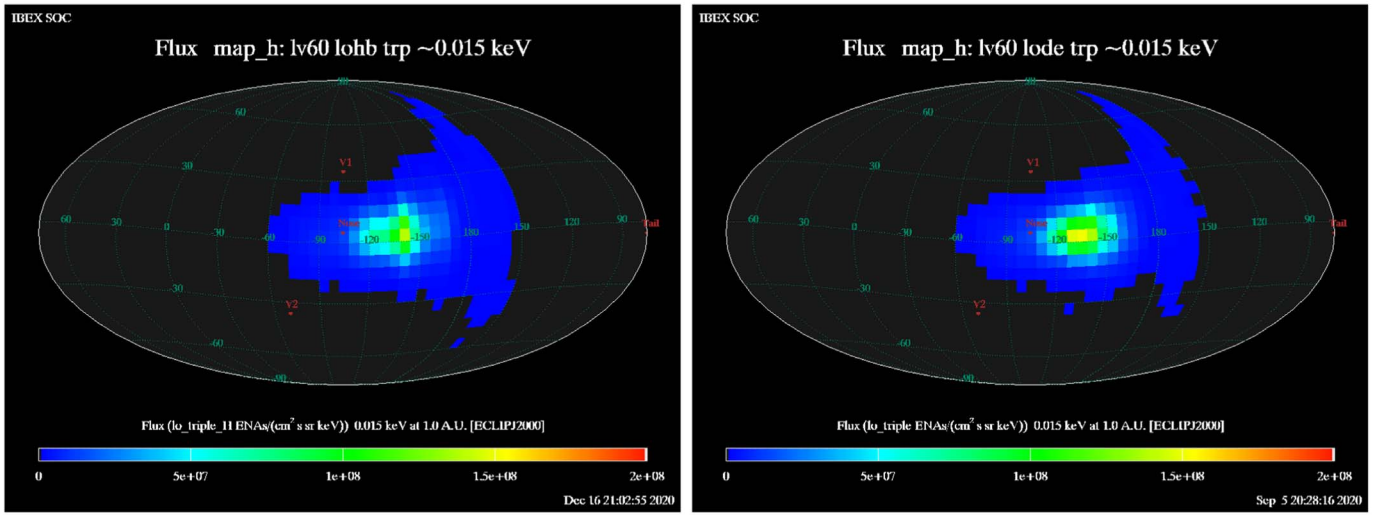
Figure 15. H⁻ count rate maps of histogram binning mode data (left panel) vs. direct event data (right panel) for energy bin 1 in the year 2009. This map is dominated by the intense signal of interstellar neutral hydrogen producing H⁻ count rates. Note the spurious shift of the peak location introduced by the change in data acquisition.
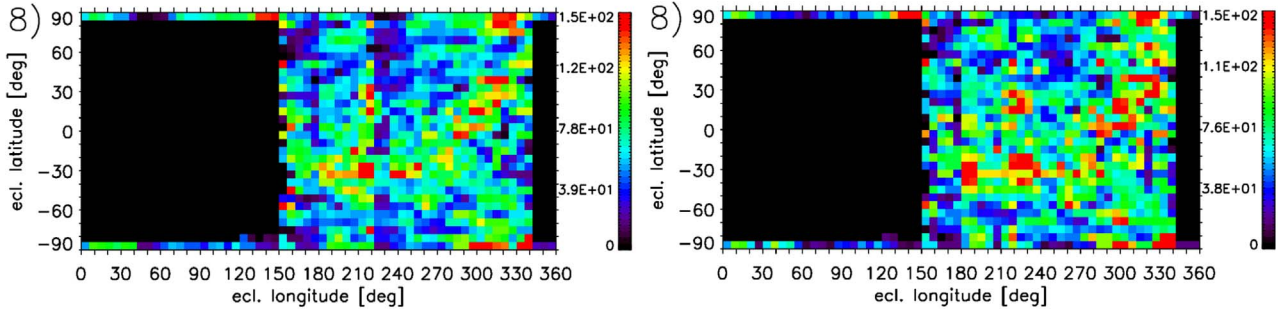

Figure 16. ENA intensity maps (in units of cm^{-2} sr^{-1} s^{-1} keV^{-1}) for "Super Good Times" (left panel) vs. "Super Better Times" (right panel) for energy bin 8 in the year 2009 for HB data, ram observations.
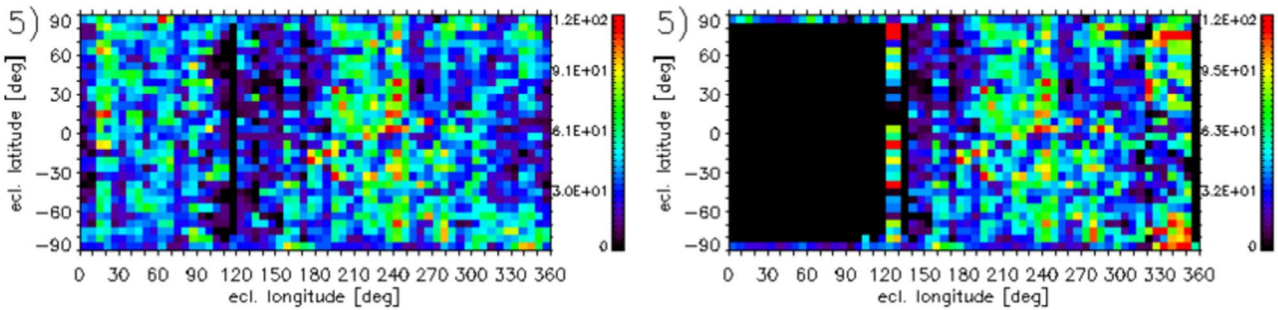

Figure 17. Combined ram and antiram map (left panel) vs. ram directions only (right panel) for energy bin 5 for the year 2014 for SC-Maps (ENA intensities in units of cm^{-2} sr^{-1} s^{-1} keV^{-1}).

Appendix B
Background

The ubiquitous background measured with IBEX-Lo was quantified by comparing ENA observations from ram and antiram directions and by averaging over quiet times in antiram direction for the lowest energy bins where neither ISN nor ENA signals are expected (see details in Galli et al. (2014)). This background is called ubiquitous because it does not exhibit seasonal or secular variations, and it cannot be removed from the data by any selection of observation period. The background changed only once during the mission, i.e., when the PAC voltage of IBEX-Lo was reduced from 16 kV to 7 kV in 2012. The ubiquitous

background is most likely a combination of ions generated inside the IBEX-Lo sensor plus an external contribution triggered by scattered solar wind, by energetic particles that hit the outer electrostatic analyzer directly, and/or by ENAs sputtering low-energy H⁻ and O⁻ from the IBEX-Lo conversion surface.

The average ubiquitous background subtracted from triple coincidence H⁻ count rates before the PAC change is listed in Table 7 (Galli et al. 2015), the one after the PAC change in Table 8 (Galli et al. 2017), the background subtracted from triple coincidence O⁻ count rates before the PAC change is listed in Table 9 (Galli et al. 2015). For IMAP-Lo, this ubiquitous background is anticipated to be less of an issue thanks to

Table 7
Ubiquitous H⁻ Background for 2008–2012 June

Energy Bin	Count Rate (s^{-1})	1σ Uncertainty
1	0.0098	0.0025
2	0.0089	0.0020
3	0.0118	0.0015
4	0.0113	0.0015
5	0.0056	0.0010
6	0.0008	0.0008
7	0	0
8	0	0

Table 8
Ubiquitous H⁻ Background for July 2012–Present

Energy Bin	Count Rate (s^{-1})	1σ Uncertainty
1	0.0067	0.0015
2	0.0075	0.0010
3	0.0076	0.0018
4	0.0074	0.0020
5	0.0012	0.0012
6	0.0002	0.0002
7	0	0
8	0	0

Table 9
Ubiquitous O⁻ Background for 2008–2012 June

Energy Bin	Count Rate s^{-1}	1σ Uncertainty
1	0.0009	0.0001
2	0.0008	0.0001
3	0.0008	0.0001
4	0.0010	0.0001
5	0.0005	0.0001
6	0.0002	0.0001
7	0	0
8	0	0

improvements in the electrode design and a lower operational temperature for IMAP-Lo compared to IBEX-Lo.

Appendix C
Survival Probabilities

Survival probabilities for the ENAs observed by IBEX-Lo were calculated identically to those computed for IBEX-Hi (McComas et al. 2020). The theory behind this calculation was presented by Bzowski (2008). The probability of an ENA being lost, deflected, or modified in terms of energy on its trajectory from 100 au heliocentric distance toward the IBEX-Lo instrument is calculated from photoionization rates, electron impact ionization rates, charge exchange rates with solar wind protons, solar radiation pressure, and solar gravity. The model of the rates of the ENA ionizing reactions (charge exchange with solar wind protons and photoionization) was adopted from Sokół et al. (2020) and from Bzowski et al. (2013) for electron impact ionization. The model of radiation pressure, which is much more important for low-energy ENAs than for those observed by IBEX-Hi, was adopted from Kowalska-Leszczyńska et al. (2020). The survival probabilities were
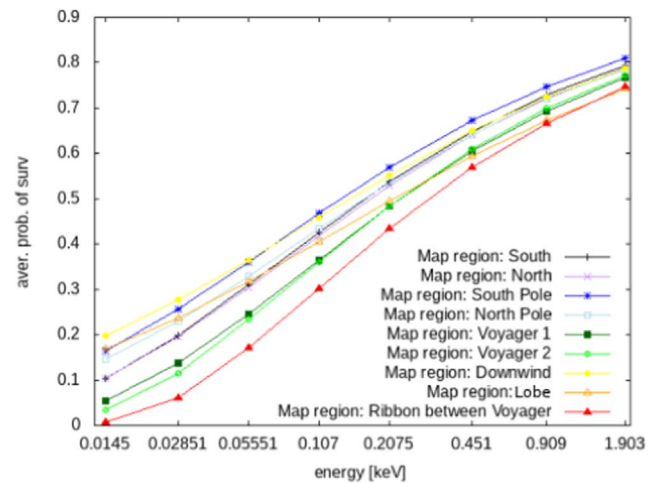

Figure 18. Spectra of the survival probabilities averaged over the entire span of the ram observations presented in this paper for the sky regions in Table 3.

calculated separately for all IBEX orbits and all energy bins. For an individual orbit, the probabilities were computed for test atoms arriving at the detector at the centers of the 6° bins distributed along the instrument scanning circle in the spacecraft inertial frame, for the energies corresponding to the center of the energy bins. They were adopted from the products used by the IBEX-Team to perform survival probability corrections, identical to that used also by McComas et al. (2020).

For the needs of this paper, we present example results, corresponding to the selected data presentation. Figure 18 presents spectra of the survival probabilities for all of the sky regions presented in Table 3 for the ram-viewing geometry. The probabilities for the sky regions were computed as mean values of the probabilities for the individual bins contained within the region and averaged over time. Because of the relatively low speeds and the related long exposures to ionization, ENAs from the lowest energy bins are attenuated the strongest, and because of the differences in the ENA orbit geometries, the differences between the probabilities for different regions may be considerable, by a factor of 2. The survival probabilities increase and the differences between regions decrease with an increase in the energy. Note that the differences between the largest and the lowest probabilities for a given sky region span about 1 order of magnitude, while the differences in the measured fluxes presented in Figure 9 reach three orders of magnitude.

The survival probabilities feature variations during the solar cycle, as shown in Figure 19. These variations are close to coherent between the energy bins, but their amplitude decreases with increasing energy, from more than a factor of 2 for the lowest energy bins down to 10%–15% for the highest energies. Solar cycle effects are clearly visible, with a clear delay in time between the lowest energies relative to the highest. This effect was already discussed by Ruciński & Bzowski (1995) in their pioneering work on modulation of hydrogen in the heliosphere during the cycle of solar activity. Because of this effect, the lowest probabilities for the highest energies occurred in 2015, but for the lowest energies in 2016. While the probabilities typically are highest during low solar activity, i.e., in 2009 and 2019 in the presented sample, there was a brief increase in 2014, i.e., shortly before the last solar maximum.
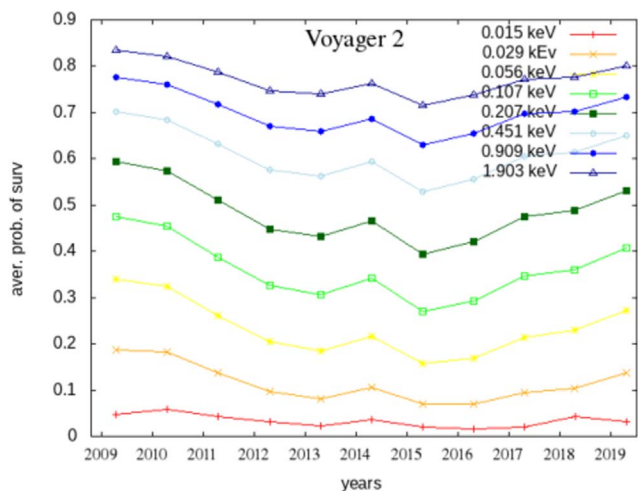
Figure 19. Time series of survival probabilities for all energy bins for the Voyager 2 region for the ram-viewing geometry.

ORCID iDs

A. Galli ⬡ https://orcid.org/0000-0003-2425-3793
P. Wurz ⬡ https://orcid.org/0000-0002-2603-1169
N. A. Schwadron ⬡ https://orcid.org/0000-0002-3737-9283
E. Möbius ⬡ https://orcid.org/0000-0002-2745-6978
R. Winslow ⬡ https://orcid.org/0000-0002-9276-9487
M. Bzowski ⬡ https://orcid.org/0000-0003-3957-2359
M. A. Kubiak ⬡ https://orcid.org/0000-0002-5204-9645
I. Kowalska-Leszczyńska ⬡ https://orcid.org/0000-0002-6569-3800
S. A. Fuselier ⬡ https://orcid.org/0000-0003-4101-7901
J. M. Sokół ⬡ https://orcid.org/0000-0002-4173-3601
P. Swaczyna ⬡ https://orcid.org/0000-0002-9033-0809
D. J. McComas ⬡ https://orcid.org/0000-0001-6160-1158

References

Bzowski, M. 2008, A&A, 488, 1057
Bzowski, M., Sokół, J. M., Tokumaru, M., et al. 2013, in Cross-Calibration of Past and Present Far UV Spectra of Solar Objects and the Heliosphere, ed. R. M. Bonnet, E. Quémerais, & M. Snow (New York: Springer), 67
Bzowski, M., Swaczyna, P., Kubiak, M. A., et al. 2015, ApJS, 220, 28
Desai, M. I., Allegrini, F., Bzowski, M., et al. 2014, ApJ, 780, 98
Funsten, H. O., Allegrini, F., Bochsler, P., et al. 2009, SSRv, 146, 75

Fuselier, S. A., Allegrini, F., Bzowski, M., et al. 2012, ApJ, 754, 14
Fuselier, S. A., Allegrini, F., Bzowski, M., et al. 2014, ApJ, 784, 89
Fuselier, S. A., Allegrini, F., Funsten, H. O., et al. 2009a, Sci, 326, 962
Fuselier, S. A., Bochsler, P., Chornay, D., et al. 2009b, SSRv, 146, 117
Fuselier, S. A., Galli, A., Richardson, J. D., et al. 2021, ApJL, 915, L26
Galli, A., Baliukin, I., Bzowski, M., et al. 2022, SSRv, 218, 31
Galli, A., Wurz, P., Fuselier, S. A., et al. 2014, ApJ, 796, 9
Galli, A., Wurz, P., Park, J., et al. 2015, ApJS, 220, 30
Galli, A., Wurz, P., Rahmanifard, F., et al. 2019, ApJ, 871, 52
Galli, A., Wurz, P., Schwadron, N. A., et al. 2016, ApJ, 821, 107
Galli, A., Wurz, P., Schwadron, N. A., et al. 2017, ApJ, 851, 2
Gomez, R. G., Fuselier, S. A., Sokół, J. M., et al. 2021, GeoRL, 48, e2021GL093695
Kornbleuth, M., Opher, M., Baliukin, I., et al. 2021, ApJ, 921, 164
Kowalska-Leszczyńska, I., Bzowski, M., Kubiak, M. A., & Sokół, J. M. 2020, ApJS, 247, 62
Kubiak, M. A., Bzowski, M., Sokół, J. M., et al. 2014, ApJS, 213, 29
McComas, D. J., Allegrini, F., Bochsler, P., et al. 2009a, SSRv, 146, 11
McComas, D. J., Allegrini, F., Bochsler, P., et al. 2009b, Sci, 326, 959
McComas, D. J., Allegrini, F., Bzowski, M., et al. 2014, ApJS, 213, 20
McComas, D. J., Bzowski, M., Dayeh, M. A., et al. 2020, ApJS, 248, 26
McComas, D. J., Bzowski, M., Frisch, P., et al. 2010, JGRA, 115, A09113
McComas, D. J., Bzowski, M., Fuselier, S. A., et al. 2015, ApJS, 220, 22
McComas, D. J., Christian, E. R., Schwadron, N. A., et al. 2018, SSRv, 214, 116
Möbius, E., Fuselier, S., Granoff, M., et al. 2007, ICRC (Mérida), 30, 841
Park, J., Kucharek, H., Möbius, E., et al. 2016, ApJ, 833, 130
Porowski, C., Bzowski, M., & Tokumaru, M. 2022, ApJS, 259, 2
Reisenfeld, D. B., Bzowski, M., Funsten, H. O., et al. 2016, ApJ, 833, 277
Reisenfeld, D. B., Bzowski, M., Funsten, H. O., et al. 2021, ApJS, 254, 40
Ruciński, D., & Bzowski, M. 1995, A&A, 296, 248
Schwadron, N. A., Möbius, E., Fuselier, S. A., et al. 2014, ApJS, 215, 13
Schwadron, N. A., Möbius, E., Leonard, T., et al. 2015, ApJS, 220, 25
SILSO, World Data Center 2008, Sunspot Number and Long-term Solar Observations, 2008-2014, International Sunspot Number Monthly Bulletin and Online Catalog (Royal Observatory of Belgium), https://www.sidc.be/silso/
Sokół, J. M., Dayeh, M. A., Fuselier, S. A., et al. 2021, ApJ, 922, 250
Sokół, J. M., McComas, D. J., Bzowski, M., & Tokumaru, M. 2020, ApJ, 897, 179
Swaczyna, P., Bzowski, M., Kubiak, M. A., et al. 2018, ApJ, 854, 119
Swaczyna, P., Kubiak, M. A., Bzowski, M., et al. 2022, ApJS, 259, 42
Swaczyna, P., McComas, D. J., Zirnstein, E. J., et al. 2020, ApJ, 903, 48
Tokumaru, M., Fujiki, K., & Iju, T. 2015, JGRA, 120, 3283
Wood, B. E., Izmodenov, V. V., Linsky, J. L., & Malama, Y. G. 2007, ApJ, 657, 609
Wu, C.-C., Liou, K., Lepping, R. P., et al. 2016, EP&S, 68, 151
Zirnstein, E. J., Heerikhuisen, J., McComas, D. J., et al. 2018a, ApJ, 859, 104
Zirnstein, E. J., Kumar, R., Heerikhuisen, J., McComas, D. J., & Galli, A. 2018b, ApJ, 860, 170
Zirnstein, J., Heerikhuisen, J., Zank, G. P., et al. 2014, ApJ, 783, 129